# MICRO-SATELLITE CAMERA DESIGN

A THESIS SUBMITTED TO
THE GRADUATE SCHOOL OF NATURAL AND APPLIED SCIENCES
OF
THE MIDDLE EAST TECHNICAL UNIVERSITY

BY

GÜLSÜM BAŞAK BALLI

IN PARTIAL FULLFILMENT OF THE REQUIREMENTS FOR THE DEGREE OF
MASTER OF SCIENCE
IN
THE DEPARTMENT OF PHYSICS

SEPTEMBER 2003

Approval of the Graduate School of Natural and Applied Sciences

Prof. Dr. Canan Özgen
Director

I certify that this thesis satisfies all the requirements as a thesis for the degree of Master of Science.

Prof. Dr. Sinan Bilikmen
Head of Department

This is to certify that we have read this thesis and that in our opinion it is fully adequate, in scope and quality, as a thesis for the degree of Master of Science.

Assoc. Prof. Dr. Akif Esendemir
Supervisor

Examining Committee Members

Prof. Dr. Bülent Akınoğlu

Assoc. Prof. Dr Gülay Öke

Assoc. Prof. Dr. Serhat Çakır

Dr. Ali Alaçakır

Assoc. Prof. Dr. Akif Esendemir

# ABSTRACT

## MICRO-SATELLITE CAMERA DESIGN

Ballı, Gülsüm Başak
M.S., Department of Physics
Supervisor: Assoc. Prof. Dr. Akif Esendemir

September 2003, 89 pages

The aim of this thesis has been summarized as the design of a micro-satellite camera system and its focal plane simulations. The average micro-satellite orbit heights ranges in between 600-850 km and obviously a multipayload satellite brings volume and power restrictions for each payload. In this work, an orbit height of 600 km and a volume of 20×20×30 cm is assumed, since minimizing the payload dimensions increases the probability of the launch. The pixel size and the dimensions of an imaging detector such as charge-coupled device (CCD) have been defined by the useful image area with acceptable aberration limits on the focal plane. In order to predict the minimum pixel size to be used at the focal plane modulation transfer function (MTF), point spread function (PSF), image distortion and aberration simulations have been carried out and detector parameters for the designed camera have been presented.

Key Words: Micro-satellite, Maksutov telescope, CCD, image quality, aberration.

# ÖZ

## MİKRO UYDU KAMERA TASARIMI

Ballı, Gülsüm Başak
Yüksek Lisans, Fizik Bölümü
Tez Yöneticisi: Doç. Dr. Akif Esendemir

Eylül 2003, 89 sayfa

Bu tez çalışmasının amacı, mikro uydularda görüntü alabilecek bir kamera tasarımı ve bu tasarımın odak düzlemi benzetişimlerini yapmaktır. Mikro uydu tanımı genelde 600-850 km yörünge yüksekliğindeki uydular için kullanılmaktadır. Bu yükseklikte görüntü alabilen optik bir sistemin boyutları algıladığı toplam ışınım miktarını etkileyeceği için önemli bir parametredir. Tasarım, 600 km yörünge yüksekliğindeki mikro uydularda 20×20×30 cm boyutlarına sığacak şekilde gerçekleştirilmiştir. Odak düzlemi detektörü olarak kullanılabilecek bir CCD nin boyutu ve piksel ebatları, odak düzlemindeki kabul edilebilir sınırlardaki sapınç miktarlarının belirlenmesiyle seçilmiştir. Minimum piksel boyutlarının belirlenmesi amacıyla odak düzleminde MTF, PSF, bükülme, saçılma benzetişimleri yapılmış ve tasarlanan kamera için dedektörün parametreleri sunulmaktadır.

Anahtar Kelimeler: Mikro uydu, Maksutov teleskop, CCD, görüntü kalitesi, sapınç

# ACKNOWLEDGEMENTS

I would like to express my gratitude to Assoc. Prof. Dr. Akif Esendemir for his guidance, for sharing his knowledge and experiences.

I would like to thank Mr. Namık Açan for his valuable discussions and encouragement.

Special thanks are due to my dear friends for their worthy supports and helpful academical contributions.

I would like to thank for my dear fairy teller.

I also wish to thank to my family and my grandmother for their understanding, full support and encouragement.

# TABLE OF CONTENTS

APPENDICES

# LIST OF TABLES

TABLE

# LIST OF FIGURES

FIGURE

.

# CHAPTER 1

# INTRODUCTION

## 1.1. General Information

Remote sensing of the Earth has long been recognized as one of the major benefits, which has resulted from the conquest of space. Orbiting satellites offer unique possibilities for monitoring the Earth's surface and atmosphere, and many programs have been established to exploit the data from remote sensing spacecrafts [1]. First artificial satellite, Sputnic, was launched in 1957 by Russia. Many satellites were launched for different purposes after Sputnic, but none of them carried an imaging system until 1970. In many parts of the world, a lot of remote sensing systems have been launched for imaging the earth, e.g. projects like LANDSAT, SPOT and IRS since 1972 [1].

In the mid-1990s, the importance of remote sensing is being increasingly emphasized with proposals for many new missions. However, conventional satellites require huge costs and long development periods. Therefore, there is consequently a need to reduce the cost of remote sensing in order to maintain the services offered by these spacecraft within tightening budgetary constraints. As a result, smaller spacecraft are gaining favor many application areas, including remote sensing. In this regard, micro-satellites have been started to observe the Earth. The design environment of a micro-satellite is very different to that of previous remote sensing satellites nowadays. However, such small vehicles present a number of extremely limiting engineering constraints like extremely limited weight, volume, power, attitude stability and communication bandwidths. In order to design the imaging payload properly, which is critical for the success of any remote sensing mission, the role of supporting systems should be understood adequately. Moreover, it is necessary to choose a camera for designing an imaging system for micro-satellites.

In line with Turkish government policy, over the last few years, the State Planning Organization and TUBİTAK have been taking steps to ensure that the country will acquire a national capability and competence in space technology. Thus TUBİTAK information technologies (BILTEN) and electronics, which is located on the campus of Middle East Technical University in Ankara, has initiated basic research into areas such as satellite design, satellite dynamics and control, space physics, etc., besides remote sensing. In 1997, Bilten applied to the Turkish Treasury and was given permission to obtain an international loan to fund the development and launch of an enhanced micro-satellite called BilSAT that would have a remote sensing capability [2].

BilSAT will have a weight of 100 kg and have an optical imaging capability. When completed, BilSAT will be launched into a Sun-synchronous orbit at an altitude of 650 km. The satellite is designed to carry digital frame cameras equipped with charge-coupled devices (CCD). A number of Turkish engineers and scientists will be directly involved in the design, building, testing and commissioning of the flight test model of the satellite. This would allow knowledge and experience to be gained in a wide range of satellite technologies in Turkey [2].

In this context, a project has been developed in the Department of Physics, METU to design a new micro-satellite camera system, which may be used in the above-mentioned micro-satellite. This camera has been designed with the help of an optical design program called ZEMAX (Focus Software, Inc., 2001), which can model, analyze, assist in the design of optical systems and can allow very rapid interactive design. This program uses ray tracing to model refractive, reflective and diffractive sequential and non-sequential optical systems.

## 1.2. Objective of the Study

The objective of this study was to design a camera system to be used in a micro-satellite which will be launched into a circular orbit at an altitude of 600 km and take images of areas with 38.5×38.5 km from the earth surface. In order to find the optimum camera system design, environmental conditions encountered at an altitude of 600 km. The weight and volume limitations of micro-satellites and the necessity of high quality images have been considered. Since the weight of the camera should not exceed the predefined about, the camera has to be as light as possible and has to be installed into a limited space in the micro-satellite. Therefore, a volume of 20×20×30 cm has been chosen to install the camera system in this study. Also considering the temperature, radiation and light attenuation limitations at that altitude, appropriate optical materials have been determined. However, both the mechanical design of this camera and the radiation effects on these optical materials in this system are not the subject of this study. Thus, the type of the camera has been chosen as a Maksutov type of objective [3], which provides the more focal length for less volume. The proposed camera system has also the ability to take panchromatic images depending on the type of the imaging detector (CCD), which has been placed on to the focal plane.

In order to obtain good quality images at the focal plane, the ZEMAX program is used to simulate the parameters like characteristics of lenses and mirrors (radius, thickness and type of glasses), as well as the position of lenses and mirrors. The simulations are repeated several times for the different beam incident angles. In addition to these simulations, the performance tests like modulation transfer function (MTF), point spread function (PSF), distortion of image and aberration have been carried out. Furthermore, the necessary calculations have been conducted to determine the properties (e.g. focal length, cardinal points, F-number, magnification, resolution and ground sample distance, etc.) of the camera system. The relation in between the pixel size of the CCD and the resolution has been determined and illustrated in the related figures. The designed camera has been optimized by those simulations and ready for construction to be used in a suitable micro-satellite.

The next chapter, the literature related to the micro-satellites and some constraints for a micro-satellite camera have been presented. The details of the camera system, which has been designed to be installed into a micro-satellite, and the computations of some physical properties have been explained in Chapter 3.

The simulations and their outputs, which have been conducted to optimize the camera system for the best image quality, have been described and discussed in Chapter 4.

Finally, in Chapter 5, the over all work has been summarized and further research possibilities have also been suggested.

# CHAPTER 2

# MICRO-SATELLITE AND LIMITATIONS OF THE IMAGING SYSTEMS

## 2.1. Definition of the Term “Micro-Satellite”

The satellites are classified according to their missions as well as their weights, which define the satellite altitudes. Although the class boundaries are not so certain the classification is shown in Table 2.1 [1].

Table 2.1. Satellite classification

| **Class** | **Weight** |
|---|---|
| Large | < 1000 kg |
| Small | > 1000 kg |
| Mini | > 500 kg |
| Micro | > 100 kg |
| Nano | > 10 kg |

What is different in the specification of a micro-satellite, as opposed to a larger conventional spacecraft, is establishing what constitutes ‘acceptable’ performances from the housekeeping systems. Given the inherent limitations on weight, size and power faced on micro-satellites, it is inevitable that many of the features of large spacecraft will not be available. Correspondingly, many of the design solutions for imaging systems on large spacecraft simply will not work on a micro-satellite due to district limitations of the micro-satellite on altitude, weight, volume, and power consumption [1].

This chapter reviews the mass, volume and power limitations for an imaging system. It also contains the effects of electromagnetic radiation and light attenuation for imaging systems in micro-satellites.

### 2.1.1. Mass Budget

By definition, the weight of a micro-satellite is between 50 to 100 kg, presenting the most obvious restriction of this class of space vehicle. While a payload-to-platform ratio of 30 % may appear low, it is in fact unusually high for a micro-satellite.

The largest contributing factor to a micro-satellite's overall mass is the structure itself. While this may appear paradoxical, a strong structure is essential if the spacecraft is to withstand the rigorous of launch, and ground handling and transport (which is possibly more stressful than the launch itself). However, striving for lower structural mass involves a delicate trade-off because of the diverse penalties incurred: reduced structural rigidity, increased risk of metal fatigue, increased complexity of manufacture due to reduced machining tolerances, reduced thermal conductivity, reduced radiation screening, etc [1].

The choice of materials and material thickness in a micro-satellite's structure is carefully considered. To achieve an efficient use of the mass, it is important to have each component fulfill as many requirements as possible. It will certainly be lighter for a single element (i.e. a suitably machined metal box) to provide, for example, structural rigidity, support of electronic circuits, thermal relief and shielding from both ionizing and non ionizing radiation, than to accomplish these goals with individual components.

Imaging instruments larger than about 20 kg simply cannot be accommodated on a 50 kg micro-satellite, and are at the limit of the capabilities of 100 kg spacecraft.

Despite the large instruments, it is possible to implement very much smaller all-electronic (i.e. mechanically passive) imaging systems, which are therefore more suited for micro-satellite applications. The dominant mass contributor to these imaging systems is generally the optics, which will need to be kept compact and lightweight to fly on these small missions. This immediately limits the scope for deploying very high resolution (long focal length) or low-light (large aperture) systems on a micro-satellite.

### 2.1.2. Structure and Volume

As the name suggests, micro-satellites are small in addition to being low mass. Given the emphasis on keeping the structural mass down, micro-satellites tend to be fairly compact and squat (close to cubic or spherical) to withstand the launch conditions. Furthermore, launch agencies rarely offer a large volume for micro-satellites launched auxiliary payloads, as most of the rocket's fairing envelope is employed by the primary customer. These factors dictate that the imaging payload must be compact light-weight.

Obviously, the imaging systems will need to have access to the outside of the spacecraft body and to be facing the Earth. However, the external surfaces are at a premium on a micro-satellite, being mainly covered with body-mounted solar panels. Given the number of other sensing systems (mainly attitude determination and control system (ADCS), but also other payloads) and communication antennas that need to occupy the remaining space, not much room is left for the imaging system and its optics.

On Surrey Satellite Technology Ltd. (SSTL) micro-satellites prior to and including micro-satellite PoSAT-1, the largest volume made available for the camera optics and electronics at the Earth-facing end of the satellite was about 260×60×40 mm.

Similarly, the maximum aperture that could be cut into the bottom of the spacecraft to accommodate a lens was less than 5 cm diameter. An additional 300×300×30 cm module tray was provided in the middle of the spacecraft stack for the imaging system's remaining (digital processing) electronics. Granted that none of these spacecraft were dedicated imaging missions, these are nevertheless tiny volumes in which to develop remote sensing capabilities, and represent a much greater limitation than the mass or other constraints.

Once again, the Cerise mission is the micro-satellite offering the most generous payload conditions. Following significant mechanical redesign and a careful re-deployment of the essential housekeeping systems, an Earth facing payload compartment has been provided, which can hold payloads occupying up to about 250×250×200 mm. Even though this volume represents a huge improvement compared to the space available on PoSAT-l, it is still a tight constraint on the design of imaging instruments.

This configuration was retained for the micro-satellite FASat-Alfa mission, which supported four cameras among the numerous payloads, sensors and antennas on the Earth-facing facet. Although the individual cameras are still very compact (130×90×60 mm excluding optics; the largest lens flown takes the dimensions to 130×90×180mm), the provision of a less cramped compartment has allowed the camera electronics to take a more natural configuration easing their manufacture and testing. On future dedicated Earth observation missions, the entirety of this payload compartment will no doubt be occupied by imaging systems [5], [6].

Therefore, to be suitable for consideration on a micro-satellite mission, the mass and volume of an imaging instrument must be kept extremely low. The mass and volume restrictions will present greater limitation on the design of the optics. It will be necessary to employ folded optics for focal lengths greater than 200-300 mm. Physical apertures greater than 15 to 20 cm will be very difficult to accommodate [1].

### 2.1.3. Power Conditioning

The power consumption of the main payload rarely consumes more than about 10 % of the spacecraft's total power budget. Given the overheads of the housekeeping systems (presumably the attitude control, transmitters, active thermal control and active mechanical systems use the lion's share of the power), there is only moderate emphasis on reducing the power consumption of the imaging payloads. Any savings made by the payloads would only be of minor benefit, and may entail some loss of performance.

With the mass and volume restrictions of micro-satellites, it is not possible for these spacecraft to carry large solar arrays or battery packs for generating and storing electrical power. Mechanical Sun-tracking arrays are too complex and massive to implement on this size of spacecraft, so the solar panels are generally body-mounted. This provides only small areas over which to collect Sunlight. Furthermore, the incident light will rarely be perpendicular to the illuminated panel, reducing the efficiency. Therefore, the power produced from a micro-satellite's solar panels will be limited.

Assuming that the transmitter of a dedicated micro-satellite draws the equivalent of a continuous 2 Watts, the total housekeeping load will be around 6 Watts. This leaves around 20 Watts for all the payloads. Fortunately, in practice, the imaging systems are generally only required for half an orbit, when the scenes below are in Sunlight. This is advantageous because when operating in Sunlight, energy is drawn straight from the solar panels without incurring any of the losses associated with the batteries. Under these circumstances, the spacecraft should be able to sustain somewhat higher payload powers, approaching 25 to 30 Watts. A 100 kg micro-satellite equipped with deployed (but not Sun-tracking) solar panels, should be able to support higher payload powers, around 50 to 70 Watts.

Fortunately, it is possible to implement all-electronic imagers with much more modest power requirements. Although the power budget of a micro-satellite is very low compared to that of a conventional remote sensing satellite, it does not appear to present as much of a constraint as the mass and volume limitations.

## 2.2. Electromagnetic Radiation and Light Attenuation

In principle, remote sensing systems could measure energy emanating from the Earth's surface in any sensible range of wavelengths. However technological considerations, the selective opacity of the Earth's atmosphere, scattering from atmospheric particulates and the significance of the data provided exclude certain wavelengths. The major ranges utilized for earth resources sensing are between about 0.4 and 12 μm (referred to below as the visible/infrared range) and between about 30 to 300 mm (referred to below as the microwave range) [19].

When sensors on satellites and aircraft record image data, it can contain errors in geometry and in the measured brightness values of the pixels because of the radiation effects. Also, light is attenuated due to atmospheric conditions.

### 2.2.1 Radiation

Radiation units are energy per unit area. Radiation flux is radiation per unit time, per area such as watts per square meter. When radiation impinges on a medium, it can be

- Transmitted (not affected)
- Reflected (e.g., a mirror) or scattered
- Absorbed

Albedo is the fraction of light that is reflected from a surface. The Earth-atmosphere albedo (% reflectance) is about 30. The average for oceans is about 6 [16].

The electromagnetic spectrum is a broad class of radiation, as illustrated in Fig. (2.1).

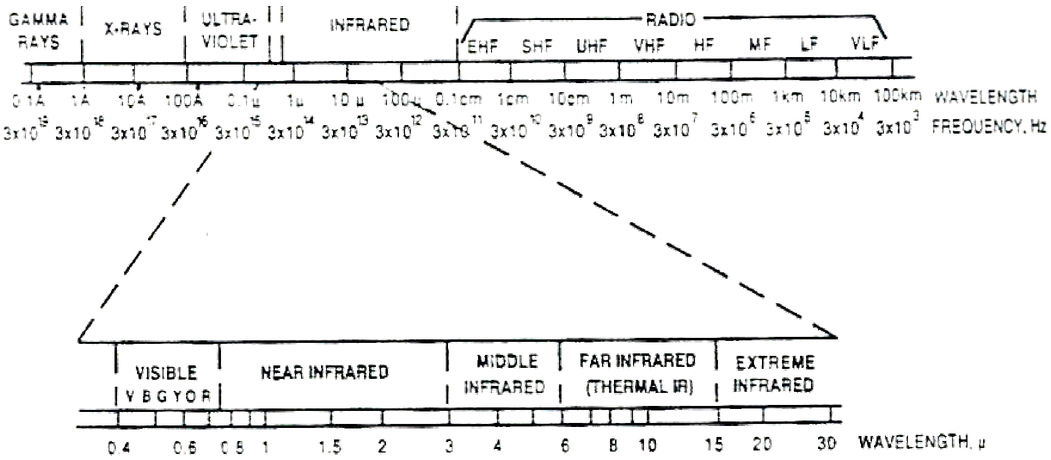

Figure 2.1. Electromagnetic spectrum [13]

For all electromagnetic radiation, the relation between the wavelength, $\lambda$, and the frequency, $\nu$, is

$$c = \lambda\nu = 2.998\times10^{8}\ \text{m/s} \tag{2.1}$$

where c is the speed of light for free space.

At any temperature above absolute zero (0 K), all matter continuously emits electromagnetic radiation. This is called thermal radiation or blackbody radiation. For a perfect blackbody, the rate of total energy emission and the energy distribution by wavelength or frequency is a function of the temperature, T. The spectral energy distribution of a blackbody is given by Planck's Law:

$$E_\lambda = \frac{2\pi hc^2}{\lambda^5}\frac{1}{e^{\frac{hc}{kT\lambda}} - 1} \tag{2.2}$$

where $E_\lambda$ is the energy per unit wavelength (also called the spectral irradiance and typically measured in W/m$^2$.µm), $\lambda$ (µm) is the wavelength, $h$ is Planck's constant

($6.626\times10^{-34}$ W.s$^2$), T is the absolute temperature, *c* is the velocity of light, and *k* is Boltzmann's constant ($1.3805\times10^{-23}$ W.s/K) [13].

### 2.2.2. Radiation Sources

- A body with T > 0 K radiates energy
- Total energy/time is sum over all $\lambda$
- Total radiation of a blackbody increases as $T^4$ according to Stefan-Boltzmann Law

  $E_{bb}(T) = \sigma T^4$ where $\sigma = 5.67\times10^{-8}$ W.m$^2$K$^{-4}$
- $\lambda_{peak}$ is inversely proportional to T according to Wien's Law

  $\lambda_{peak}T = 2898$ µm.K
- Sun: $T_{BB} \approx 6000$ K $\lambda_{peak}$ in visible, ultraviolet
- Earth: $T_{BB} \approx 253$ K ($T_{actual} \approx 288$ K) $\lambda_{peak}$ in infrared

The absorption of radiation by the atmosphere is a function of wavelength. By the Stephan-Boltzmann relationship, the Sun puts out $(T_{BB\ sun}/\ T_{BB\ earth})^4 \cong 188{,}000$ as much energy as the Earth. Since the contribution of the Earth's $T_{BB}$ to the flux used for imaging is very little. It will be neglected throughout this work.

The average insolation is 1360 W/m$^2$, which is known as solar constant. About 49% of the incoming solar radiation is in the visible range 400-700 nm. About 9% is in the ultraviolet range, and the remaining 42% is in the long-wave infrared range and beyond [16].

The solar constant has had many different numerical expressions throughout the years, during the time period of 1978 through 1998, the mean value of daily averages for the solar constant from six different satellites yielded a solar constant of 1366.1 W/m$^2$. This same source offers a minimum-maximum range of the readings for 1363-1368 W/m$^2$ [17]. Adjustments yielded "a solar constant" calculated to 1366.22 W/m$^2$ [15].

Water vapor and $CO_2$ have high absorption in the infrared range; so more of the energy radiated by the Earth-atmosphere system is absorbed percentage-wise than the incoming radiation. In Fig. (2.2), the partition of an arbitrary 100 units of incoming solar radiation showing percentage absorbed and scattered in various ways [16].

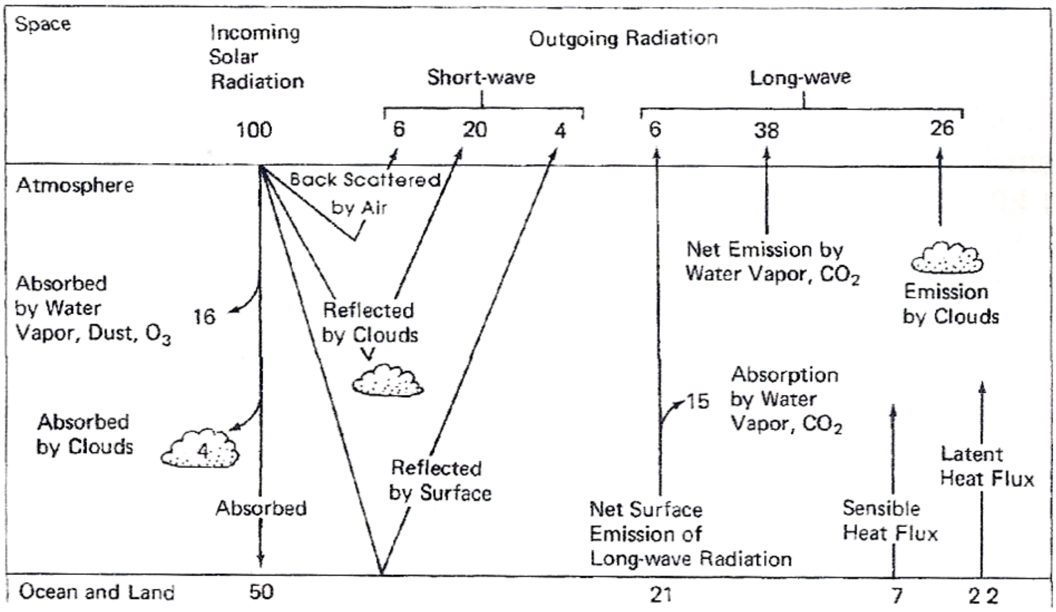

Figure 2.2. Incoming solar radiation [16]

Therefore, some of the insolation received by the Earth will be absorbed by the atmosphere, reflected by the atmosphere, absorbed by the Earth's surface, and reflected back to space by the Earths surface as shown in Fig. (2.3) [18].

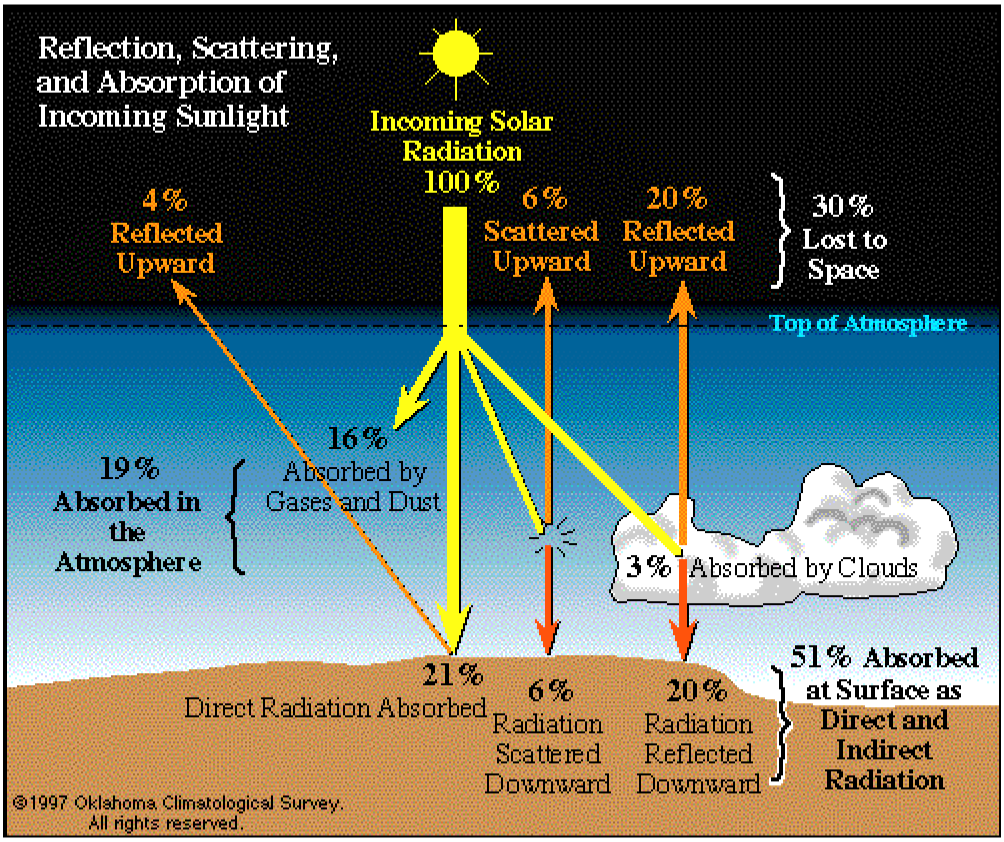

Figure 2.3. Albedo [18]

Imaging systems, which are used in earth observation satellites, do not take sunlight directly from the sun. They observe reflected sunlight from the earth. As discussed in section 2.2.1, it is called albedo so only 30% of the solar energy arrives the telescope. In this study, this system has been used only for visual and near infrared bands to observe the earth. This means camera takes less than 30% of the solar energy. If better images are desired, the diameter of the telescope should be increased in order to gather more light. On the other hand, larger aperture means more weight which is a fundamental problem of satellite optical system. For this reason, the traditional imaging systems, which are useful for larger satellites, are not exploited on micro-satellites where mass and volume are limited. As discussed in section 2.1, mass and volume restrictions are the most important limitations for the design of the optics. Therefore, as pointed by Marc Fouquet, the mass and volume of an imaging instrument must be kept extremely low. In order to provide this situation, folded optics is used for the design.

# CHAPTER 3

## DESIGNING A CAMERA OBJECTIVE

In past space applications, camera systems have used lenses (refractive systems), but now catadioptric is used mostly so the same optical train can collect both visual and IR signals [13]. Optical systems which are constructed with the combinations of mirrors and lenses are called as catadioptric optics.

There are several ways to describe an optical system. Parallel rays of light falling on a perfect lens will all converge at the focal point, whose distance from the lens is called the focal length, $f$. Effective focal length of an optical system determines the length of the optics system, which is defined by the lens surface's radius of curvature. The surface of a parabolic reflector may be defined as an equation of the parabola with focus $f\,(a,0)$ and the directrix the line with equation $x = a$, [13].

$$y^2 = 4fx \tag{3.1}$$

When a lens forms the image of an extended object, the amount of energy collected from a small area of the object is directly proportional to the area of the clear aperture, or entrance pupil, of the lens. At the image, the illumination (power per unit area) is inversely proportional to the image area over which this object is spread. Now the aperture area is proportional to the square of the pupil diameter (D), the image area is proportional to the square of the image distance, or focal length. Thus, the square of $f/D$ is a measure of the relative illumination produced in the image [4].

The ratio of the focal length to the clear aperture of a lens system is called the relative aperture, F-number. The illumination (power per unit area) in an image is inversely proportional to the square of this ratio. The relative aperture is given by:

$$\text{F - number} = \frac{\text{effective focal length}}{\text{clear aperture}} = \frac{f}{D} \tag{3.2}$$

As an example, an 8-inch focal length lens with a 1-inch clear aperture has an F-number of 8; this is customarily written F/8 or F: 8.

Another way of expressing this relationship is by the numerical aperture (NA), which is the index of refraction of the medium in which image lies times the sine of the half angle of the cone of illumination.

$$\text{NA} = \text{n} \sin \alpha \tag{3.3}$$

Numerical aperture and F-number are obviously two methods of defining the same characteristic of a system. Numerical aperture is more conveniently used for systems that work at finite conjugates (such as microscope objectives), and the F-number is appropriately applied to systems for use with distant objects (such as camera lenses and telescope objectives). For aplanatic systems (i.e., systems corrected for coma and spherical aberration) with infinite object distances, the two quantities are related by:

$$\text{F - number} = \frac{1}{2\text{NA}} \tag{3.4}$$

The terms “fast” and “slow” are often applied to the F-number of an optical system to describe its “speed”. A lens with a large aperture (and thus a small F-number) is said to be “fast”, or to have a high “speed”. A smaller aperture lens is described as “slow”. This terminology derives from photographic usage, where a larger aperture allows a shorter or faster exposure time to get the same quantity of energy on the film [4].

The focal length of a lens determines the magnification of the image, and thereby dictates the spatial resolution in an electronic camera which uses a CCD [1].

$$\text{magnification} = m = \frac{f}{h} = \frac{r}{R} \tag{3.5}$$

where $h$ is the distance from the satellite to the object, $r$ is the radius of the detector array in the image plane, and $R$ is the radius of the object, with both image and object measured perpendicular to the line of sight (see Fig. 3.1). The magnification or scale is the ratio of the image size to the object size. It is ordinarily a very small number for satellites. The scale on the image plane is expressed as "1 cm equals to $x$ km on the ground." [13].

Figure 3.1 shows how the focal length of the lens $f$ and the satellite's altitude above the ground $h$, combined with the CCD sensor's dimensions, determine the coverage area and pixel resolution of the final image.

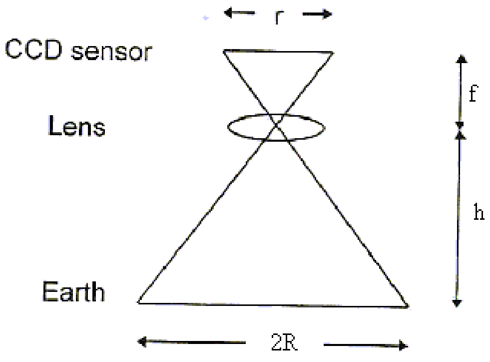

Figure 3.1. Relationship between camera characteristics and spatial resolution

Because it is simple to calculate, this is the widely used definition of spatial resolution for remote sensing cameras. In reality, the true resolution of a camera is rather more difficult to establish. Each element in the optical system, including the sensor, will introduce point spreading losses which reduce the actual ground resolution from this theoretical value.

There is a simple relationship between the dimensions of CCD, the focal length and the orbital altitude define the imaging system's resolution and field of view. Given that the orbit of a micro-satellite will be beyond the control of the camera designer, and the dimensions of the selected CCD are fixed, the only real variable in the system is the lens. Therefore, the choice of lens focal length effectively determines the imager's resolution [1]. Before discussing the results of this relationship, camera that had been designed for micro-satellite was explained below.

Since it is easy to reflect IR and visual energy, optical systems can be made compact by using folded reflective telescopes. They consist of a larger primary reflector and a smaller secondary mirror whose boresight blockage does not materially affect the incoming signal strength as seen Fig. (3.2) [13].

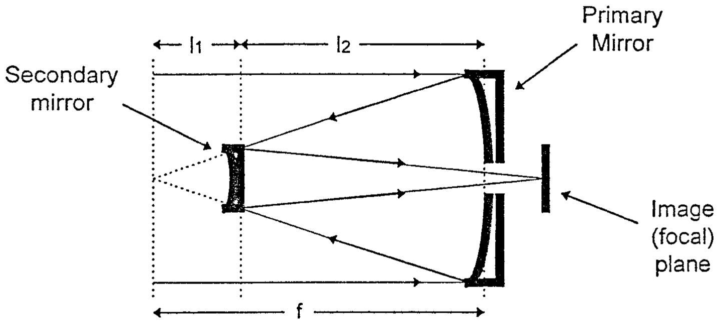

Figure 3.2. A typical Cassegrainian folded optics telescope system [13]

### 3.1. Camera Description

In order to provide a suitable camera system for restricted number of photons that would be imaged on an orbiting satellite, it was necessary to employ a fast camera.

A camera has been designed as a Maksutov type of objective to be used in a micro-satellite which will be launched into a circular orbit at an altitude of 600 km and take images from the earth surface. This objective consists of a plane mirror, two parabolic mirrors and two lens groups that are named corrected and relay lenses as shown in Fig (3.3).

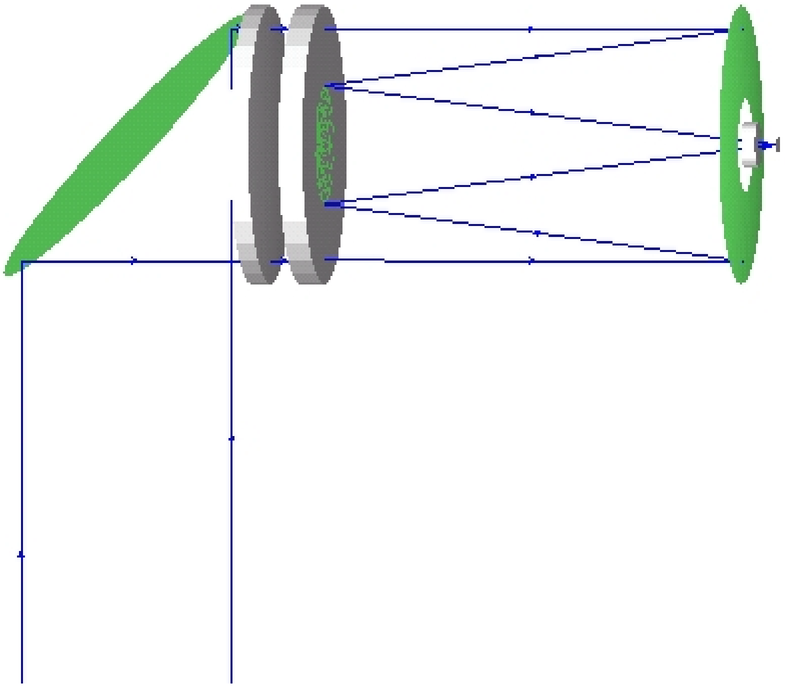

Figure 3.3. Designed camera

Increase on the demand for imaging in nonvisual bands of the spectrum, i.e., the ultraviolet and infrared regions, has resulted a corresponding increase in the use of reflecting optics This is due primarily to the difficulty in procuring completely satisfactory refractive materials for these regions, and secondarily, to the fact that many of the applications permit the use of relatively unsophisticated mirror systems [4].

Reflecting surfaces generated by rotation of the conic sections (circle, parabola, hyperbola, and ellipse) share two valuable optical properties. First, a point object located at one focus is imaged at the other focus without spherical aberration. The paraboloid of revolution, described by the Eq. (3.1) has one focus at *f* and the other at infinity, and is thus capable of forming perfect (diffraction limited) images of distant axial objects. The second, characteristic of conic sections is that if the aperture stop is located at the plane of a focus, as shown in Fig. (3.4), then the image is free of astigmatism.

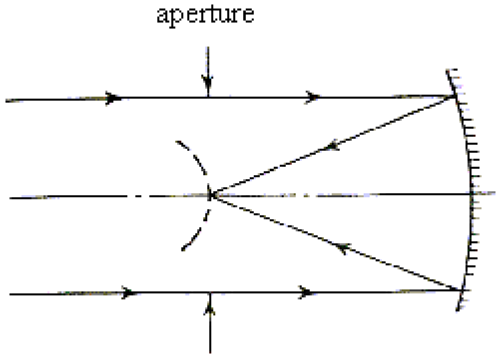

Figure 3.4. Parabolic reflector [4]

However, the paraboloid is not completely free of aberrations; it has both coma and astigmatism. Since it has no spherical aberration, the position of the stop does not change the amount of coma. The amount of astigmatism is modified by the stop position. When the stop is at the focal plane, the astigmatism is zero and the image is located on a spherical surface of radius *f*, as shown in Fig. (3.4) [4].

This design includes two concave parabolic mirrors, which are named primary and secondary mirror, for good focusing. The diameter of the large main mirror or primary mirror is 60 mm and the radius of curvature is 405 mm. The secondary mirror, which has the diameter, is 28 mm and the radius of curvature is 10000 mm. Positioned within the beam of the large mirror and inside its focal plane, the secondary mirror reshapes the beam of the large mirror into one of a narrower aperture that passes through a hole cut in the main mirror. The primary mirror is relatively massive so it is a rigid body. The weight of a camera increases very rapidly with weight of the mirrors.

In order to fit the camera to the assumed volume as discussed in Sec. (1.2.), the plane mirror with a diameter of 80 mm is used.

Group of corrector lenses, which have been used to increase the effective area, have been designed by using two single lenses. Both of them are concave-convex lenses. They are also called positive Meniscus lenses. Table 3.1 shows the properties of these two selected lenses. Refractive index of glasses is taken for wavelength 0.587562 μm.

Table 3.1. Properties of corrector lenses

| Lens | Radius 1 (mm) | Radius 2 (mm) | Thickness (mm) | Diameter (mm) | Glass | Refractive Index |
|---|---|---|---|---|---|---|
| I | -2310.0 | -558.0 | 5.0 | 60.0 | BK7 | 1.5168 |
| II | -659.0 | -10000.0 | 5.0 | 60.0 | BK7 | 1.5168 |

When it is desired to carry an image through a relatively long distance and the available space limits the diameter of the lenses, which can be used, a system of relay lenses must be used [4]. In this study, these lenses have been designed to be achromat for minimum chromatic aberration, so the more clear images formed on the focal plane. The characteristics of the achromatic lenses are shown in Table (3.2).

Table 3.2. The characteristics of achromatic lenses

| Lens | Radius 1 (mm) | Radius 2 (mm) | Thickness (mm) | Diameter (mm) | Glass | Index |
|---|---|---|---|---|---|---|
| III | -40.0 | 85.0 | 1.5 | 10.0 | SF8 | 1.6889 |
| IV | 85.0 | -300.0 | 1.5 | 10.0 | BK7 | 1.5168 |

With those selected components, mass limitation has been overcome and weight of the mirrors and the lenses has been computed to be 71.911 g.

This optic system projects photons arriving from the scene into a focused image on the CCD sensor.

## 3.2. Brief Description of CCD Architectures

The introduction of area detectors, specifically, CCDs allowed the design of an imager capable of imaging large areas of the Earth with every pixel within the image exposed at the same instant of time [21]. There are numerous texts dealing with the general theory of operation of charge-coupled devices [22], [23], and it is unnecessary to reiterate these here in any detail. Nevertheless, a brief description of certain aspects of area-array CCDs is necessary because these factors are highly relevant in the design of remote sensing systems.

The principal of image-sensing CCDs is the combination of the photosensitive nature of a semiconductor with their behavior as analog shift registers. As photons strike the surface of a semiconductor, they produce into electron-hole pairs, generating an electronic current. In this respect, CCDs are similar to other silicon photo-detectors. However, instead of producing a DC current, each photosite[*] within the CCD traps these electrons into a charge packet. By integrating the electrons over a period of time, the array of charge packets records the spatial variations in luminous intensity of the image focused onto the sensor [1].

The majority of CCDs have their photosensitive area arranged as a series of electrically isolated columns (the sensing registers) of photosites with a single row (the readout register) across the bottom of the sensor. To read the charge packets collected by the sensor, all the columns will be shifted down by one place, with the contents of the bottom-most photosite of each column falling into the horizontal readout register. The readout register is then driven rapidly to move the charge packets towards the output amplifier. When one line has been completely read out, the columns are again driven to load the next row into the readout register. This cycle is repeated until all the charge packets associated with the photosites have been transferred to the output. In designing the two-dimensional lattice of photosites in CCD, and implementing the sequential readout of the charge packets, it is possible to generate an electronic signal representative of the scene viewed.

As charge packets are transferred within the CCD, they are physically moved across the surface of the silicon lattice towards the output amplifier. Because the entire surface of a CCD is covered by photosensitive silicon, these charge packets will continue collect any incident photons as they are being moved. Unfortunately, these extra photons will have no correlation to those originally captured by the photosites, resulting in noise. Given the column architecture of the CCD, these spurious photons cause a vertical smearing of the recorded image.

To remain radiometrically faithful to the scene, it is therefore important that each charge packet contains a large majority of electrons recorded by the original

---

[*] CCDs contain a regular array of tens of thousands of tiny light-sensitive photosites formed on a silicon "chip". In an ideal CCD, every photosite would have exactly the same sensitivity, but in the real world, each photosite is unique [23]. A photosite refers to the physical detector on a CCD.

photosite, with as few additional spurious electrons as possible. To eliminate the smearing effect, it is necessary to use a shutter to prevent any additional photons from striking the CCD once integration has terminated. In many instances this shuttering is accomplished with an external mechanical shutter, identical to those used in film photography or cinematography.

Alternatively, many CCDs implement a form ‘electronic shuttering’ internally, without having recourse to mechanical systems. This is performed by storing the charge packets in optically shielded buffers located on the surface of the CCD. Once a charge packet is safely in a shielded buffer, it will not collect any further photons, and can be read out without being subject to any further smearing (with some limitations). While most CCDs are similar in the way they record incoming photons as charge packets, it is the storage (or lack thereof) and read-out processes, which makes them different, and determines their suitability for various applications, including satellite remote sensing [1].

### 3.3. Calculations

The assumption of paraxial rays greatly simplifies the description of the progress of rays of light through an optical system, because trigonometric terms do not appear in the equations. For many purposes, this treatment is sufficient. In practice, rays of light contributing to an image in an optical system are, in fact, usually rays in the near neighborhood of the optical axis. If the quality of the image is to be improved, however, ways must be found to reduce the ever-present aberrations that arise from the presence of rays deviating, more or less, from this ideal assumption. To determine the actual path of individual rays of light through an optical system, each ray must be traced, independently, using only the laws of reflection and refraction together with geometry. This technique is called as ray tracing because it was formerly done by hand, graphically, with ruler and compass, in a step-by-step process through an accurate sketch of the optical system. Today, with help of computers, the necessary calculations yielding the progressive changes in a ray’s altitude and angle is done more easily and quickly. Graphics techniques are used to actually draw the optical system and to trace the ray's progress through the optical system on the monitor [7]. Zemax is a program, which can model, analyze, and assist, in the design of optical systems.

As discussed in section 3.1, the camera system is designed for a micro-satellite which will be launched into a circular Earth orbit at an altitude of 600 km in order to take images from the earth surface.

The following parameters are calculated for the designed camera system at wavelength 587 nm, where $f$ is the effective focal length of the system and $D$ is aperture diameter

$f = 231.9524$ mm

$D = 60$ mm

The calculations of the other parameters for the optical performance of this system (magnification, F-number, etc.), resolution, dimensions of CCD, integration time are given in following section. In addition to these calculations, position of the image, which has been computed by using matrix method, is given by Appendix B.

### 3.3.1.Optical Design

#### 3.3.1.1. Calculation of Resolution

The Rayleigh limit describes the ultimate resolving power of an optical instrument in terms of the wavelength of light "$\lambda$", for the ultimate resolving power that equation must be satisfied

$$\Delta\theta = 1.22\frac{\lambda}{D} \tag{3.6}$$

where $\Delta\theta$ is the minimum field of view angle for each pixel. Fig. (3.5) shows the relation in between the pixel cell size $x$, which satisfies the Rayleigh criteria and the ground displacement $r$, which is imaged by a single pixel.

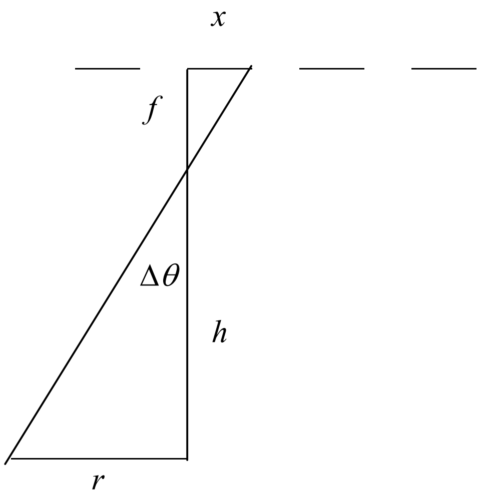

Figure 3.5. The minimum field of view angle

$$\Delta\theta = \frac{r}{h} \text{ (since } \Delta\theta \text{ is a very small angle)} \tag{3.7}$$

using Eqs. (3.6) and (3.7),

$$r = 1.22\frac{\lambda h}{D} \tag{3.8}$$

Using the Fig. (3.5),

$$\frac{f}{h} = \frac{x}{r} \tag{3.9}$$

where $h$ is altitude of the satellite.

$D = 60$ mm

$f = 231.952$ mm

$h = 600$ km

Resolution is calculated for the shorter wavelength 770 nm. For other wavelengths see Fig. (3.6).

$$r = 1.22\frac{0.770\times10^{-6}\times600\times10^{3}}{60\times10^{-3}}$$

$$r = 9.394 \text{ m} \tag{3.10}$$

$r$ that is found by Eq. (3.8) is the minimum longitudinal resolution which is defined by Rayleigh criteria of the designed optical system.

Using Eq. (3.5) or (3.9), minimum pixel size of the CCD may be written as

$$x = \frac{fr}{h} \tag{3.11}$$

$$x = \frac{231.952\times10^{-3}\times9.394}{600\times10^{3}}$$

$$x = 3.631 \ \mu\text{m}$$

The minimum pixel size, which may be used, is found to be 3.631 μm for the designed camera.

Substituting to Eq. (3.8) in Eq. (3.11),

$$x = 1.22\frac{f\lambda}{D} \tag{3.12}$$

The relation in between the pixel size and CCD pixel resolution may be found by Eq. (3.12). Fig. (3.7) shows this relation.

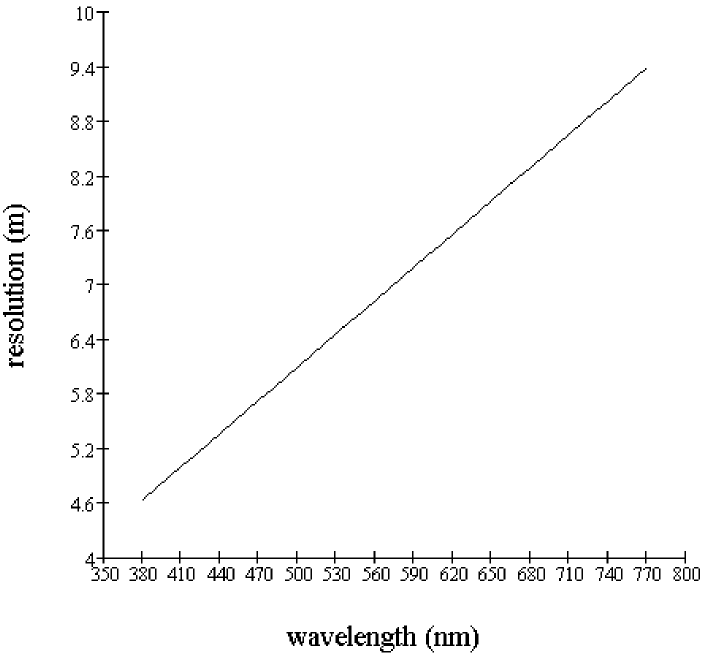

Figure 3.6. Resolution vs. wavelength

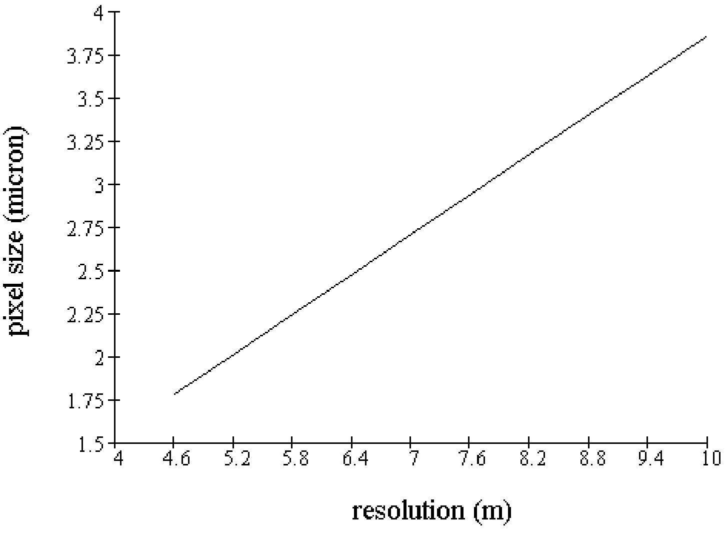

Figure 3.7. Resolution vs. pixel size

The field of view of the CCD is given by the effective focal length and the size of the CCD. For the rest of calculations, it is assumed that 4096×4096 pixels CCD with pixel size of 3.631 μm used on the focal plane of the designed system.

The diagonal length of this CCD ($d_{CCD}$) is given by

$$d_{CCD} = \sqrt{2} \times 4096 \times 3.631 \times 10^{-3} = 21.036 \text{ mm} \tag{3.13}$$

The angular coverage ($\theta$) $d_{CCD}$ on the ground may be written as,

$$\theta = 2 \tan^{-1}\left( \frac{1}{2} \frac{d_{CCD}}{f} \right) \tag{3.14}$$

$$\theta = 2 \tan^{--1}\left( \frac{1}{2} \frac{21.036 \times 10^{-3}}{231.9524 \times 10^{-3}} \right)$$

$\theta$ is found to be $5.192^{\circ}$

This corresponds to an on-ground distance ($d_{ground}$):

$$\tan\theta = \frac{d_{ground}}{h} \tag{3.15}$$

$d_{ground} = 54.415$ km

That match of the diagonal displacement on the ground corresponds to a square area 38.477 km on each side.

$$\frac{d_{ground}}{\sqrt{2}} = 38.477 \text{ km} \tag{3.16}$$

One problem with imaging is coping with image-blur due to the motion of the satellite [20]. For this reason, the camera's integration time must be kept sufficiently short to prevent blurring due to the motion of the satellite. The amount of the electrons collected in the CCD cells is linearly proportional to the integration time ($t_{int}$). The integration time can be calculated as follows.

$R_{earth-mean} = 6371\,\text{km}$

$G = 6.673 \times 10^{-11}\ (\text{m}^3/\text{kgs}^2)\ \text{or}\ (\text{Nm}^2/\text{kg}^2)$

$M_{earth} = 5.977 \times 10^{24}\ \text{kg}$

At 600 km the displacement from the center of the Earth to the satellite ($r_{earth}$):

$$r_{earth} = 6371 + 600 = 6971\,\text{km} \tag{3.17}$$

$$\text{Gravitational Acceleration: } a_g = \frac{GM}{r_{earth}{}^2} \tag{3.18}$$

$$a_g = \frac{6.673 \times 10^{-11} \times 5.977 \times 10^{24}}{\left(6971 \times 10^3\right)^2} = 8.207\ \text{m/s}^2$$

$$\frac{mv^2}{r_{earth}} = mg \Rightarrow v = \sqrt{r_{earth}\, g} = \sqrt{r_{earth}\, a_g} \tag{3.19}$$

$$v = \sqrt{6971 \times 10^3 \times 8.207} = 7564.054\ \text{m/s} = 7.564\ \text{km/s} = v_{AC}$$

$v_{AB}$ : velocity of satellite with respect to earth

$v_{AC}$ : velocity of satellite with respect to space

$v_{BC}$ : velocity of earth with respect to space

$$v_{AB} = v_{AC} - v_{BC} \tag{3.20}$$

(It is assumed that velocity vector of satellite is parallel to the velocity vector of the Earth surface.)

$R_{earth\text{-}equatorial} = 6378140\,\text{m}$

$$2\pi R = 40075035.54\,\text{km} \tag{3.21}$$

$$v_{BC} = \frac{40075035.54}{24 \times 3600} = 0.464\ \text{km/s}$$

Using Eq. (3.16), the orbital speed of the satellite at 600 km is found as,

$v_{AB} = 7.564 - 0.464 = 7.100\,\text{km/s}$

by using the calculated resolution in Eq. (3.10), the integration time may be computed as

$$r = vt \Rightarrow t_{\text{int}} = \frac{r}{v} \tag{3.22}$$

$$\frac{9.394}{7100.223} = 1.323 \times 10^{-3}\ \text{s}$$

Therefore, the satellite will cover 9.394 m on the ground in 1.323 milliseconds.

As it was known, the ratio of the focal length to the optical aperture, known as the F-number, defines the brightness of an optical system and how much light it collects. Smaller F-number indicates a larger aperture and a brighter image (i.e. it captures more photons). The F-number calculations presented in Appendix C.

Paraxial magnification of this system has been computed as fallows,

$$m = \frac{h_i}{h_o} = \frac{s_i}{s_o} \tag{3.23}$$

$h_i = 3.092$ mm

$h_o = 8 \times 10^6$ mm

where $h_i$ and $h_o$ are heights of image and object, $s_i$ and $s_o$ are image and object distances from the designed system. Magnification of the designed system is calculated from Eq. (3.23), then

$m = -\dfrac{3.092}{8 \times 10^6} = -3.865 \times 10^{-7}$ so, the image is real.

Angular magnification $m_A$,

$$\tan\alpha = \frac{h_o}{h} = \frac{8}{600} \Rightarrow \alpha = 0.763\,^{\circ}$$

$$\tan\theta = \frac{h_i}{\text{Exit Pupil Position}} = \frac{3.92703}{-50.9017} \Rightarrow \theta = 3.476^{\circ}$$

$$m_A = \frac{\theta}{\alpha} = -4.551\,^{\circ} \tag{3.24}$$

In these calculations, the pressure and temperature variation has been ignored, at 600 km altitude, but a micro-satellite exposes to this variation. If one wants to compare with the results of this variation effects on the optical parameters of the designed camera and the results that obtained in this section, both of them is given by Appendix D.

### 3.3.2. The Total Energy Incident on CCD

The optimum CCD for the designed optical system, is found to be 14.875×14.875 millimeter square image-plane consist of 4096×4096 pixels where each light-sensitive cell is 3.631×3.631 μm square. The amount of light flux focused on the CCD is dependent proportionally on the aperture area.

Considering radiometric performance, which is great importance for spaceborne instruments operating in the visible spectral range [25], the total energy incident on each CCD pixel is computed as follows.

The total incident energy ($E_i$) from approximately 38.5×38.5 km area at a distance 600 km to the optimum CCD surface may be written as:

$$E_i = \frac{A \times \Phi \times a \times d^2 \times \varepsilon_o}{2 \times h^2 \times n^2} \tag{3.25}$$

where $A$ is the imaged area on the earth surface, Φ is the solar flux, $a$ is the albedo of the earth, $d$ is the pupil radius, $\varepsilon_o$ is the efficiency of the designed camera, $h$ is the altitude of the satellite and $n$ is the number of pixels per row of the CCD. The total efficiency of the designed camera is found to be 0.85 (see Sec. (4.6)).

Then:

$$E_i = \frac{(38.477\times10^3)^2 \times 1366.22 \times 0.3 \times (30\times10^{-3})^2 \times 0.85}{2\times(600\times10^3)^2\times4096^2}$$

$$E_i = 3.843\times10^{-11} \text{ W/pixel}$$

Since the integration time is found in Sec. (3.3.1.1), energy per pixel ($E_p$) may be calculated as,

$$E_p = E_i \times t_{\text{int}} \tag{3.26}$$

$$E_p = 3.844\times10^{-11}\times1.323\times10^{-3} = 5.084\times10^{-14} \text{ J/pixel}$$

By mixing and matching technologies from disparate imaging architectures, Kodak Company has created a front-illuminated full-frame CCD technology with peak quantum efficiency* over 85% [26]. Taking the average quantum efficiency of a CCD ($\varepsilon_c$) as 0.70 in the visual band of electromagnetic spectrum, number of electrons ($n_e$) per pixel may be calculated as,

$$E_p\times\varepsilon_c = 5.084\times10^{-14}\times0.70 = 3.559\times10^{-14} \text{ J/pixel} \tag{3.27}$$

It is assumed that the average photon energy ($E_{ave}$) is equal to the energy of 500 nm may be calculated from Eq. (3.24) where h is Planck constant, and ν is frequency.

$E_{ave} = h\nu$ (3.28)

$\lambda = 500\ \text{nm} \Rightarrow \nu = c/\lambda = 5.996\times10^{14}\ \text{s}^{-1}$

$E_{ave} = 3.972\times10^{-19}$ J

$$n_e = \frac{E_p \times \varepsilon_c}{E_{ave}} \tag{3.29}$$

$n_e = \dfrac{3.559\times10^{-14}}{3.972\times10^{-19}} = 89585$ electron/pixel during the integration time

For the shorter wavelength 770 nm, $n_e = 137960$ electron/pixel

Integrated solar flux between the wavelengths 380 and 770 nm can be calculated from Eq. (2.2),

$$\int_{380\,\text{nm}}^{770\,\text{nm}} E_\lambda d\lambda = \frac{2\pi hc^2}{\lambda^5} \cdot \frac{r^2}{R_{sun-earth}} \frac{1}{e^{\frac{hc}{kT\lambda}} - 1} \tag{3.30}$$

From this computation, the solar flux is found 623.973 W/m$^2$ for visible region. Therefore it is obtained $1.625\times10^{-14}$joule per pixel and 40914 electrons are produced for each pixel during the integration time. This value is above the background level and quite enough for imaging with a good signal to noise ratio.

The CCD output can be increased by increasing the integration time and long integration times are generally used for low light level operation. However, this approach is ultimately limited by dark current leakage that is integrated along with the photocurrent and strongly with velocity of satellite. With a large pixel (24 μm square), a dark current density of 1000 pA/cm$^2$ produces 36000 electrons/pixel/s [22].

---

[*] Quantum efficiency is the ratio between the number of photons arriving on the CCD and the collected photoelectrons, it's function of the wavelength (and also of the temperature).

# CHAPTER 4

# SIMULATIONS OF DESIGNED CAMERA

Because the purpose of an imaging system is to extract necessary information from an image, the application determines the required image quality. The imaging ability of a system is the result of the imaging ability of the components. Any imaging system needs illumination, a lens, a camera, and either a monitor or a computer/capture board to store the images.

Simulations include aberrations, modulation transfer function (MTF), spot diagrams, and many other physical parameters. The results of the simulations have been interpreted basing on the graphics and discussed how image quality has been obtained.

## 4.1. Transfer Functions

Characterization of the imaging capacity of an optical system by simply citing its resolving power does not give an adequate assessment of the system's performance. The preferred criterion of performance is the optical transfer function (OTF), which is a function of the spatial frequency $\upsilon$ of the sine-wave pattern. To test an optical system properly, objects having both high and low spatial frequencies are required. As usual, low spatial frequencies are sufficient to image the gross details of an object, while high spatial frequencies are required to produce the finer details [7], [4].

The OTF is a complex function [7]. The real part of the OTF is the modulation transfer function (MTF) and the imaginary part is the phase transfer function (PTF). The PTF represents the commensurate relative phase shifts that are in centered optical systems occur only off-axis [8]. One advantage of this transfer function is that each independent component of a complete system, from the atmosphere to the detector, has its own OTF, and the system OTF is the product of the separate OTFs for geometric aberrations, random wavefront error, and blurring due to image motion. The response of the system to an incident wavefront is determined by the system OTF comprising all these factors [27].

### 4.1.1. Modulation Transfer Function

The modulation transfer function can be defined as a quantitative description of the image formation power of an optical imaging system bearing in mind all aberrations. MTF describes the ability of a lens or system to transfer object contrast to the image. Curves can be associated with the subsystems that make up a complete electro-optical or photographic system. MTF data can be used to determine the feasibility of overall system expectations. In order to determine this function, increasingly finer grids are imaged by an optical system and their modulation (contrast) in the image plane of the imaging system is measured. The fineness of the grid is given in lines per mm and is called spatial frequency $\upsilon$. Modulation (contrast) $M$ is defined as:

$$M = \frac{I_{\max} - I_{\min}}{I_{\max} + I_{\min}} \tag{4.1}$$

In this equation, $I_{\max}$ and $I_{\min}$ are the image illumination levels. [9], [10].

If one express the contrast in the image as a “modulation”, given by the above equation, the modulation can be plotted as a function of the number of lines per millimeter in the image, as indicated in Fig. (4.1.A). The intersection of the modulation function line with a line representing the smallest amount of modulation, which the system can detect, will give the limiting resolution of the system. The curve indicating the smallest amount of modulation detectable by a system or sensor (i.e., the threshold) is often called an AIM curve, where the initials stand for the aerial image modulation required to produce a response in the system or sensor. The modulation threshold usually rises with spatial frequency.

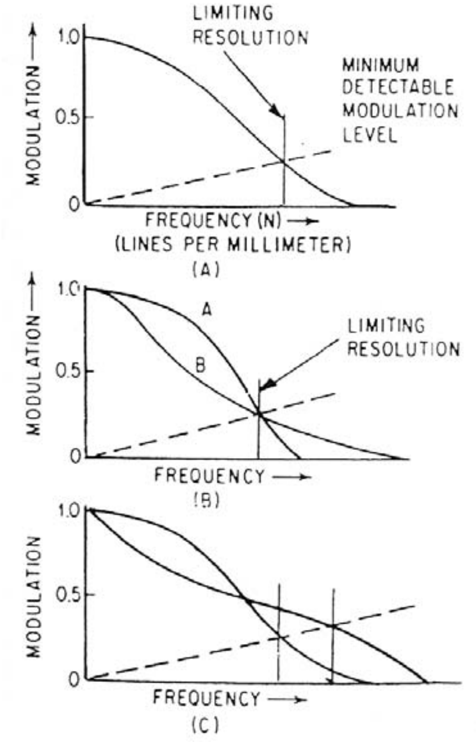

Figure 4.1.Plots of the image modulation [4]

It should be apparent that the limiting resolution does not fully describe the performance of the system. Fig. (4.1.B) shows two modulation plots with the same limiting resolution, but with quite different performances. The plot with the greater modulation at the lower frequencies is obviously superior, since it will produce crisper, contrastier images. The type of choice one is usually faced with in deciding between two systems is less obvious. Consider Fig. (4.1.C), where one system shows high limiting resolution and the other shows high contrast at low target frequencies. In cases of this type, the decision must be based on the relative importance of contrast versus resolution in the function of the system.[*]

The modulation transfer function is the ratio of the modulation in the image ($M_i$) to that in the object ($M_o$) as a function of the spatial frequency of the sine-wave pattern.

$$\mathrm{MTF}(\upsilon)=\frac{M_i}{M_o} \tag{4.2}$$

A plot of MTF against frequency $\upsilon$ is thus an almost universally applicable measure of the performance of an image-forming system [4].

With severe defocus, some of the curves show a negative value for the MTF. This indicates that the phase shift in the image is 180° and that the image is light where be dark and vice versa. This is known as spurious resolution since a line pattern can be seen, but it is not a true image of the image [4].

Small aberrations in the imaging devices and optical elements cause the MTF to decrease with increasing spatial frequency. The overall number of pixels in the imaging device sets the limiting resolution point.

Determination of MTF at various spatial frequencies, like the curves shown in Fig. (4.2), allows a more complete evaluation of system performance than resolution alone. All curves approach the MTF of 1 as the spatial frequency approaches zero

---

[*] The Strehl definition is the ratio of the light intensity at the peak of the diffraction pattern of an aberrated image to that at the peak of an aberration-free image, and is one of the many criteria that have been proposed for image evaluation. It can be computed by calculating the volume under the (three-dimensional) modulation transfer function and divided by the volume under the curve for an

axis where they can no longer resolve the data at that spatial frequency called cut-off frequency. Cut-off frequency of the designed camera is found to be 275.406 by using the pixel size.

This figure also indicates the designed camera's averaged values of MTF at wavelengths 486 nm, 550 nm, 587 nm and 656 nm for the rays between the center of the optical axis and edge of the optical axis. A black curve which is the diffraction limited of this system shows the best performance. The rays come from the center of the optical axis provide the better performance than the edge of the optical axis.

---

aberration-free lens. A similar criterion for quick general evaluation of image quality is the normalized area under the modulation transfer curve.

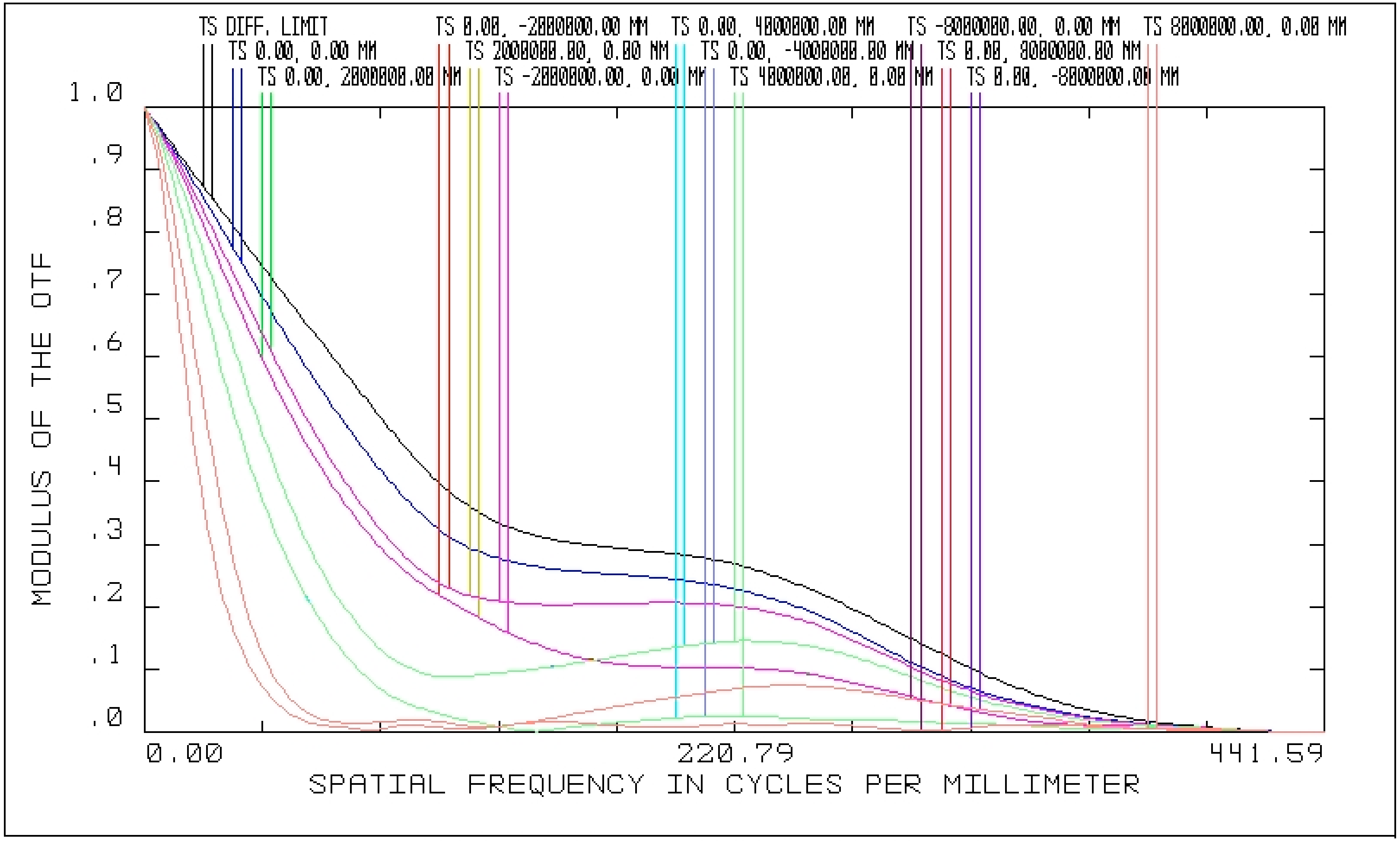

Figure 4.2. MTF of the designed camera system

### 4.1.2. Point Spread Function

The characteristics of the image of a point source object formed by a perfect optical system are completely described by the point spread function (PSF) and quantities derivable from it. One of the quantities derived from the PSF is the encircled energy fraction (EE), which is defined as the fraction of the total energy in the image enclosed within a circle of radius *r* centered on the PSF peak; for a circular or annular aperture this is the fraction of the total energy in the image within a circle of a given radius centered on the PSF. The intensity in units of flux per unit area at a point on the image is directly proportional to the PSF, while the average intensity over a centered portion of an image depends on both the PSF and EE [27].

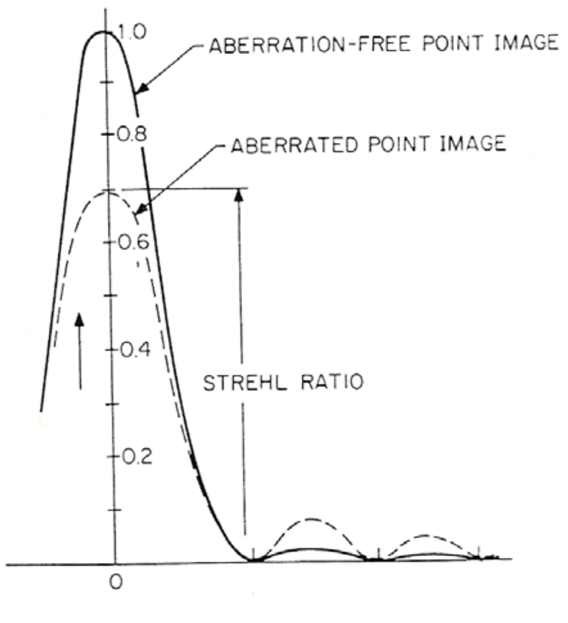

Figure 4.3. Point spread function [4]

There is a relation between the Strehl ratio and PSF, when reducing this ratio pattern of PSF is smoothed. The Strehl ratio is the illumination at the center of the airy disc for an aberrated system expressed as a fraction of the corresponding illumination for a perfect system as shown in Fig. (4.3) [4].

A common convention is to consider a system as diffraction limited if the Strehl ratio is greater than or equal to 0.8 [27]. The smaller values of the Strehl ratio do not correlate well with image quality.

Fig. (4.4) indicates the normalized PSF at polychromatic wavelength for the designed camera. The following figure shows the aberrated point image, so it defines the Strehl ratio whose value is 0.830. At wavelength 0.587 μm this value is 0.994.

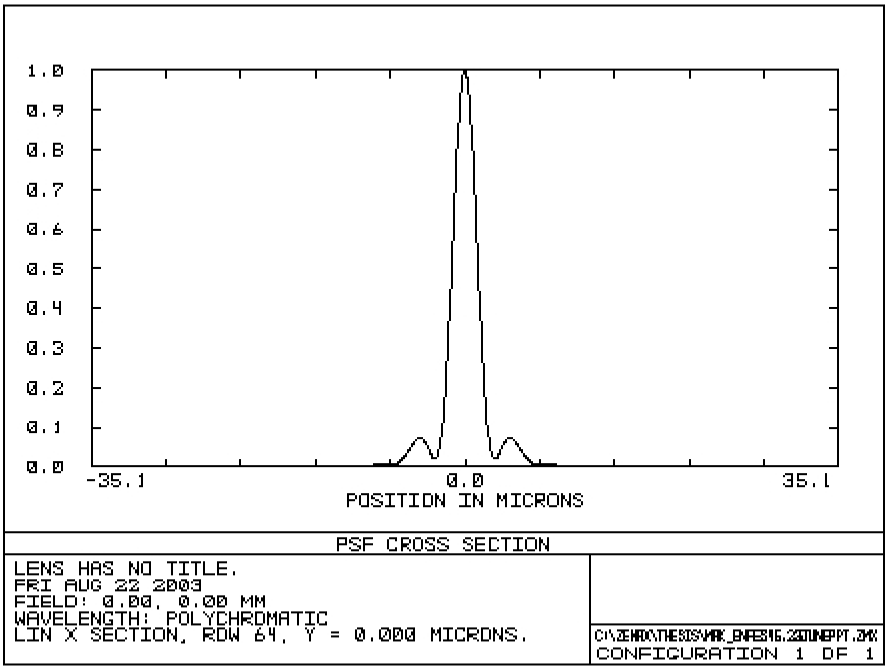

Figure 4.4. The normalized PSF for designed camera

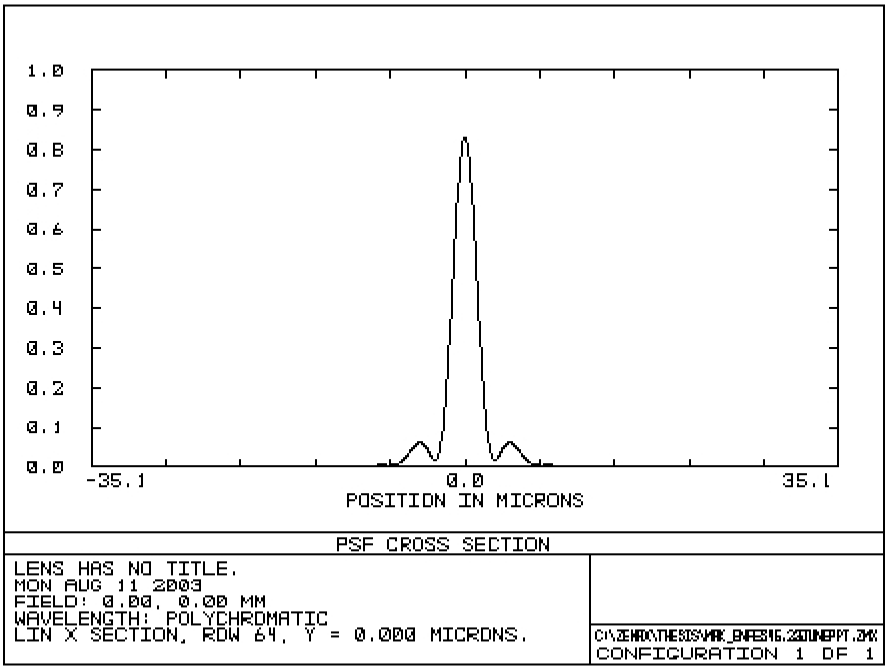

Figure 4.5. PSF of the designed camera

There is a relation between the airy disc and Strehl ratio as defined above, this is given in Table (4.1).

Table 4.1. Strehl ratio and airy disc

| Strehl Ratio | % Energy in Airy Disc |
|---|---|
| 1.00 | 84 |
| 0.99 | 83 |
| 0.95 | 80 |
| 0.80 | 68 |
| 0.4 | 40 |
| 0.1 | 20 |
| 0 | 10 |

This relation also corresponds the total efficiency of the power as will be discussed in Sec. (4.6).

As the results of these graphics, the image quality of the designed camera is said to be best. However, when the rays come from the edge of the optical axis, Strehl ratio decreases and its value is 0.078673 as shown in Fig. (4.6).

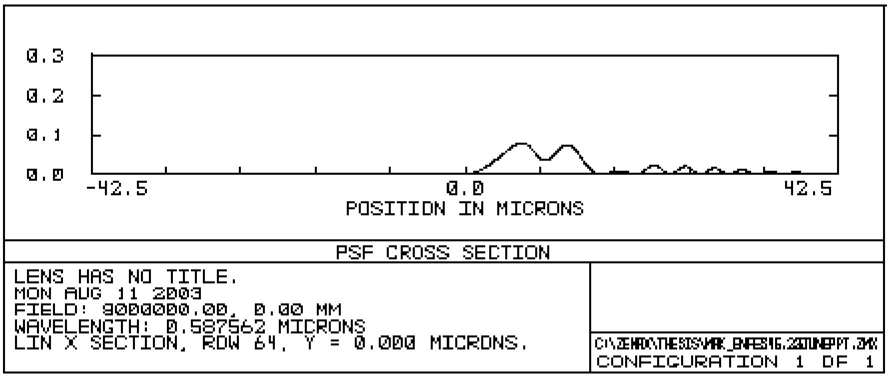

Figure 4.6. PSF for the marginal rays of the designed system

## 4.2. The Spot Diagram

When the aberration exceed the Rayleigh limit by several times, diffraction effects are relatively insignificant and the results of geometrical ray tracing may be used to predict the appearance of a point image with a fair degree of accuracy. This is done by dividing the entrance pupil of the optical system into a large number of equal areas and tracing a ray from the object point through the center of the each of the small areas. The intersection of each ray with the selected image is plotted, and since each rays represents the same fraction of the total energy in the image, the density of the points in the plot is a measure of the power density (irradiance, illuminance) in the image. Obviously the more rays that are traced, the more accurate representation of the geometrical image becomes [4]. Spot diagram is a plot of the intersection coordinates in the reference planes of rays traced through the lens or system from a single object point. The two reference planes usually chosen are the entrance pupil plane and paraxial image plane. The rays traced from the object point are usually chosen so as to form a uniform pattern of intersection with the entrance pupil plane while the resulting image is represented by the ray intersections in the paraxial image plane [28].

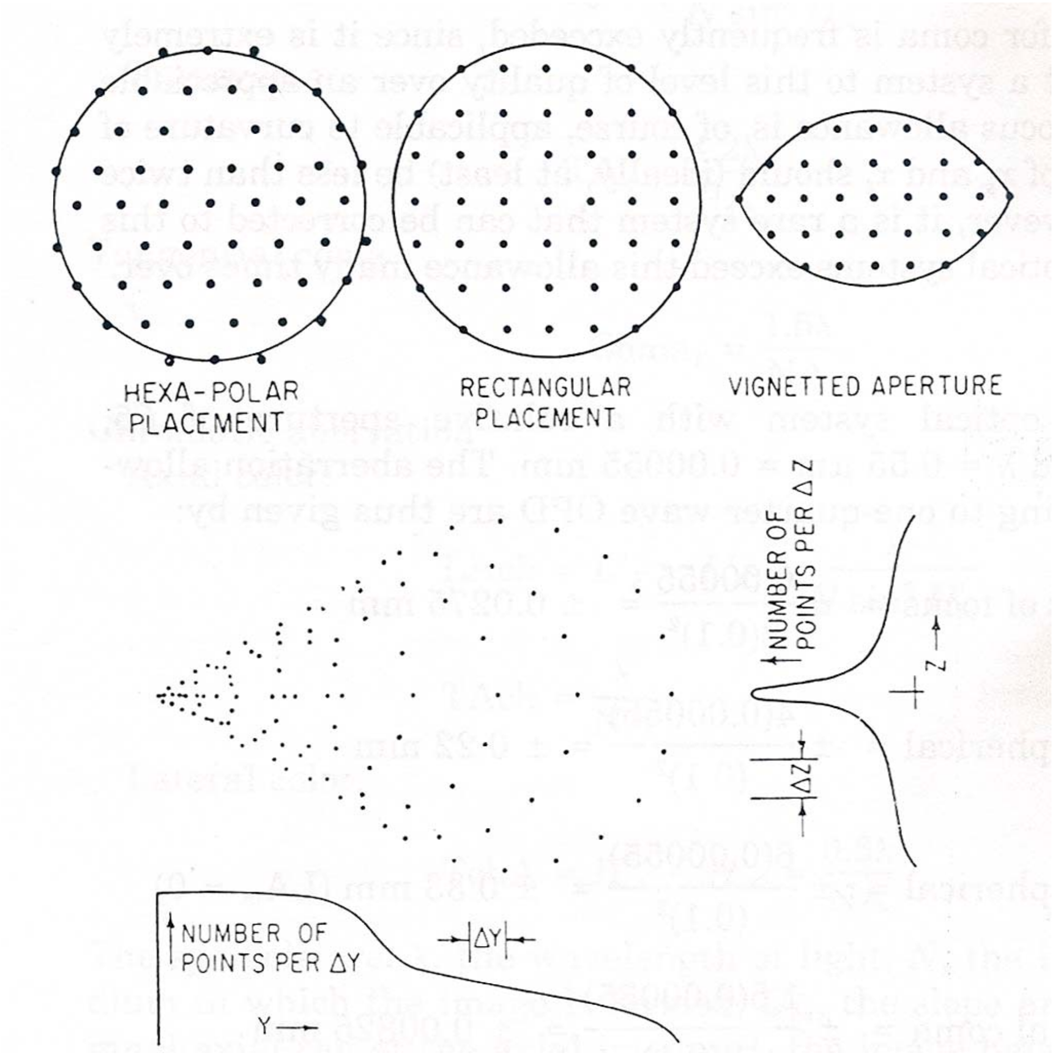

Figure 4.7. Several methods of spot diagram [4]

Fig. (4.7) indicates several methods of placing the rays in the entrance pupil and shows an example of a spot diagram [4].

The spot diagram indicates how well the lens concentrates the energy from the object point into an image point. In a theoretically perfect geometrical image all the spots would be concentrated at a point. However, in the case of the image due to a perfect optical system, the geometrical image is only an approximation; the actual image formed would be larger than a point due to diffraction effects [28].

For an accurate analysis, the effects of wavelength on the energy distribution must also be considered. This is accomplished by tracing additional rays at different wavelengths; the variation of system sensitivity with wavelength may be taken into account by tracing fewer rays in the less-sensitive wavelengths [4].

In order to interpret the spot diagram, it is often considered as a point spread function and is converted into a graph of modulation transfer function (MTF) plotted against spatial frequency.

The spot diagram shows what the image looks like and the density of points in the spot diagram tells how bright the image at that location as discussed in beginning this section. Fig. (4.8) shows the camera's spot diagram for the rays, which coincides with the optical axis of the designed camera. RMS radius and airy disc are useful to interpret this diagram.

The RMS spot size is the root-mean-square radial size. The distance between each point and the reference point is squared, and averaged over all the rays, and then the square root is taken. The RMS spot size gives a rough idea of the spread of the rays, since it depends upon every ray. The GEO spot size only gives information about the ray, which is farthest from the reference point [24].

The airy disc radius calculated is given by

$$r_{airy} = 1.22\lambda \frac{f}{D} \qquad (4.3)$$

The airy disc gives an idea of the scale of the plot. For example, if all rays are well within the airy disc, then the system is often said to be “diffraction limited”. If the RMS spot size is significantly larger than the airy disc radius, then the system is not diffraction limited.

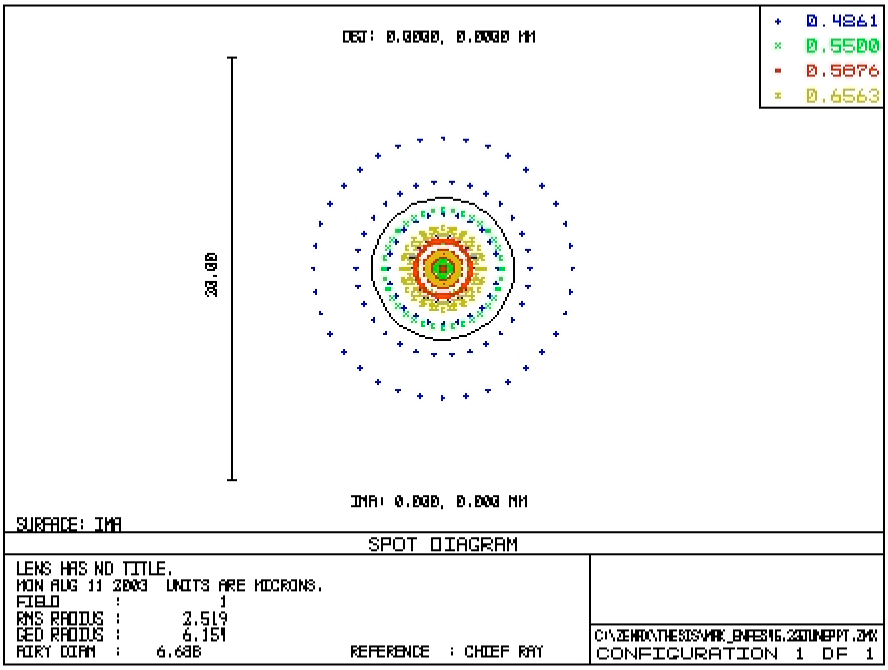

```
LENS HAS NO TITLE.
MON AUG 11 2003   UNITS ARE MICRONS.
FIELD      :          1
RMS RADIUS :      2.519
GEO RADIUS :      6.151
AIRY DIAM  :    6.638                REFERENCE   : CHIEF RAY
C:\ZEMAX\THESIS\MRK_BNFES16.23JUNEPPT.ZMX
CONFIGURATION 1 OF 1
```

Figure 4.8. Spot diagram of the designed camera

In Fig. (4.8), the camera is not diffraction limited for wavelength 486 nm. However, it is said to be diffraction limited for the other three wavelengths.

RMS radius (see Fig (4.8)) found as 2.519 microns; this RMS radius is the minimum resolution of the designed optical system resolution (9.394 m) and pixel dimensions (3.631 μm) of CCD as discussed in Chapter 3. Therefore, 1 μm on the focal plane corresponds to a distance of 2.587 m. on the ground. Then RMS radius of the system equals the 6.514 m on the ground. Airy disc radius of the camera can be computed using Eq. (4.3) as follows for wavelength 587 nm and the entrance pupil diameter has been taken 50 mm to bound the aberrations sourced by the margin rays.

$r_{airy} = 1.22 \times 0.5876 \times 4.664 = 3.344\mu\text{m}$, (diameter of the airy disc is 6.688 μm)

In following figures show the spot diagrams of the designed camera for the rays between the center of the optical axis and edge of the optical axis at wavelength 587 nm. In these positions the camera is not diffraction limited except the Fig. (4.9 first diagram), which is same as the Fig. (4.8.).

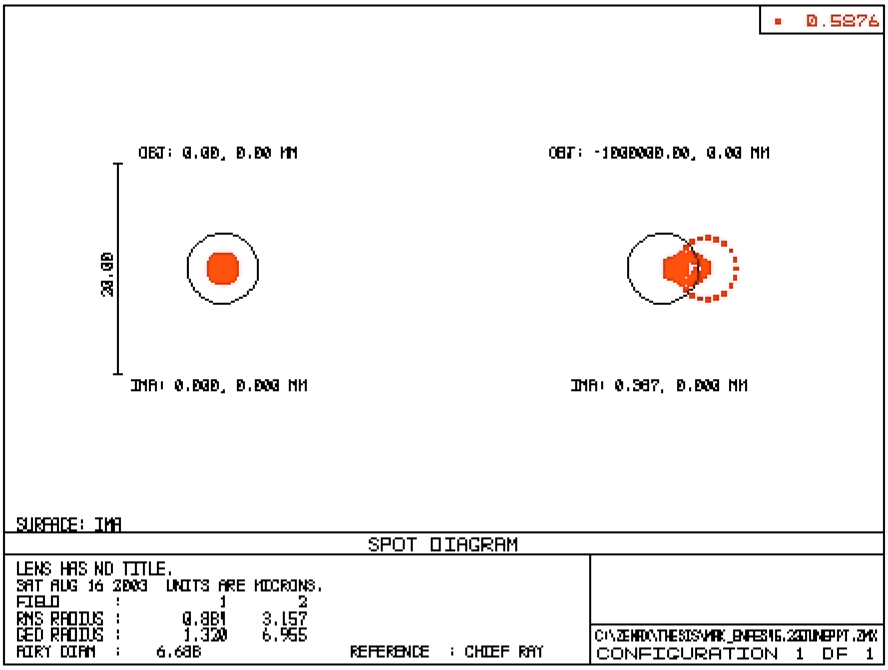

Figure 4.9. Spot diagrams of the designed camera from the center of the optical axis to edge of the optical axis

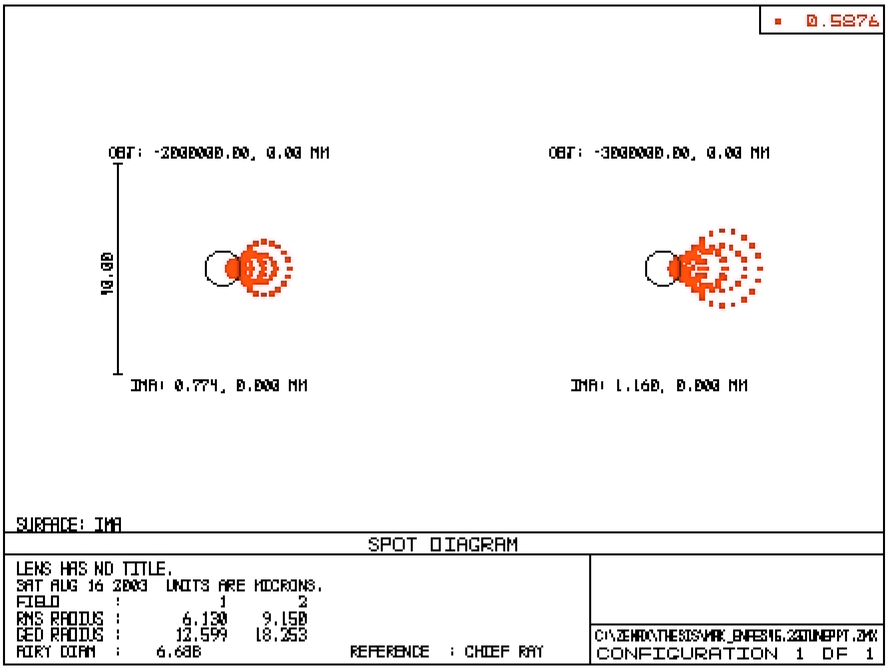

```
LENS HAS NO TITLE.
SAT AUG 16 2003  UNITS ARE MICRONS.
FIELD       :        1        2
RMS RADIUS  :    6.130    9.150
GEO RADIUS  :   12.599   18.253
AIRY DIAM   :   6.638                REFERENCE  : CHIEF RAY
```

Figure 4.10. Spot diagrams through the edge of the optical axis

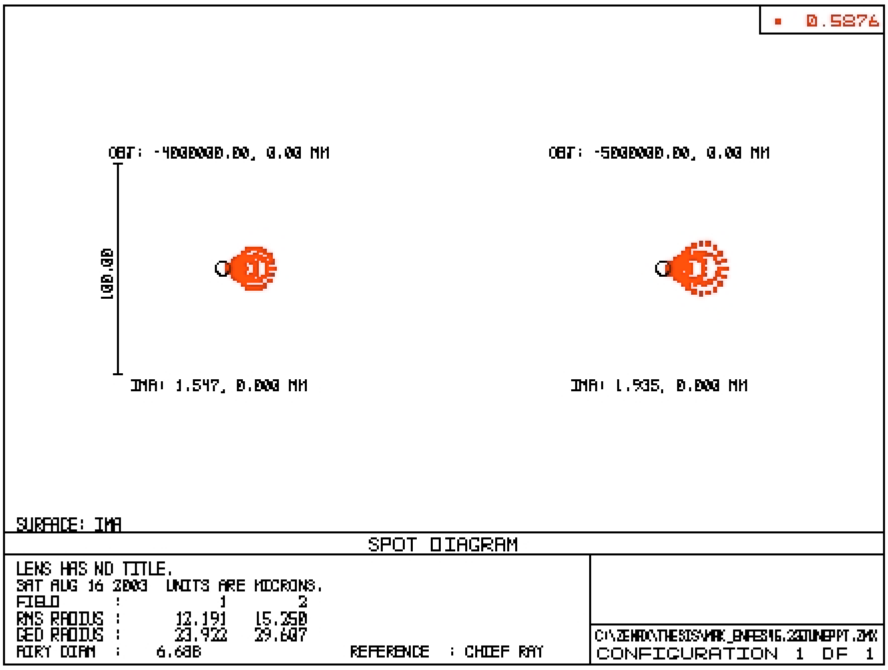

```
LENS HAS NO TITLE.
SAT AUG 16 2003  UNITS ARE MICRONS.
FIELD       :        1        2
RMS RADIUS  :   12.191   15.250
GEO RADIUS  :   23.922   29.607
AIRY DIAM   :   6.638                REFERENCE  : CHIEF RAY
```

Figure 4.11. Spot diagrams through the edge of the optical axis

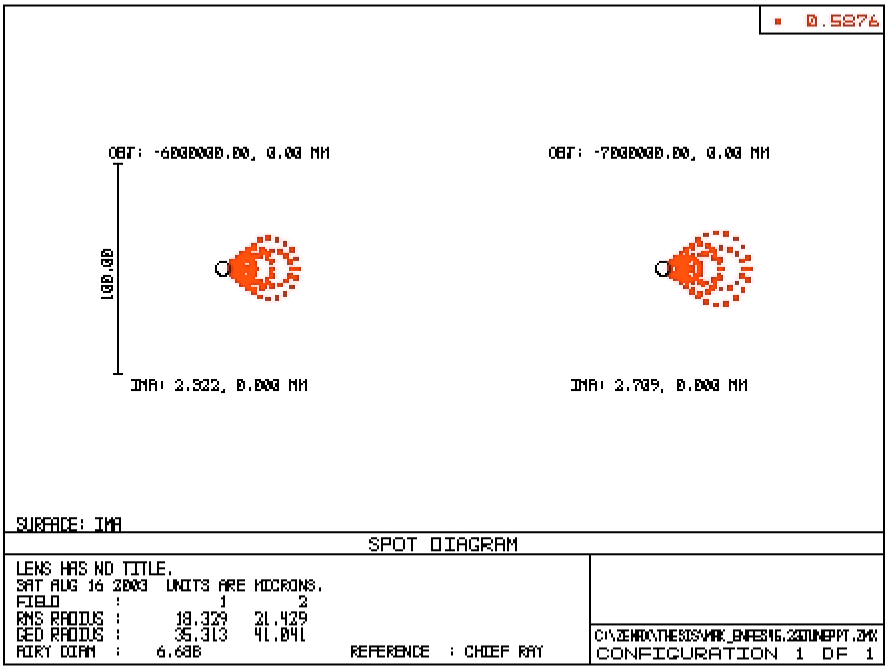

```
LENS HAS NO TITLE.
SAT AUG 16 2003   UNITS ARE MICRONS.
FIELD       :        1         2
RMS RADIUS  :     18.329    21.429
GEO RADIUS  :     35.313    41.041
AIRY DIAM   :    6.688                  REFERENCE   : CHIEF RAY
```

Figure 4.12. Spot diagrams through the edge of the optical axis

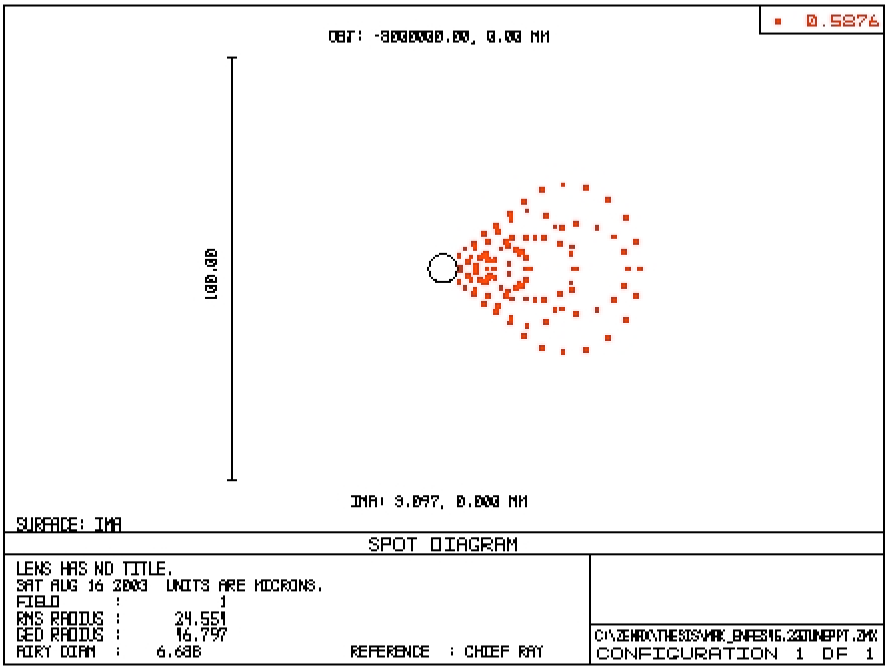

```
LENS HAS NO TITLE.
SAT AUG 16 2003   UNITS ARE MICRONS.
FIELD       :        1
RMS RADIUS  :     24.551
GEO RADIUS  :     46.797
AIRY DIAM   :    6.688                  REFERENCE   : CHIEF RAY
```

Figure 4.13. Spot diagram of the designed camera at the edge of the optical axis

When the values of the RMS radius increase, resolution limit decreases. If the technology had a curved CCD, this situation would not be important.

### 4.3. Field Curvature

The field curvature plot shows the distance from the currently defined focal (image) plane to the paraxial focal plane as a function of field coordinate. The tangential data are the distances measured along the Z-axis from the currently defined focal plane to the paraxial focal plane measured in the tangential (YZ) plane. The sagittal data are the distances measured in the plane orthogonal to the tangential plane. The base of the plot is on axis, and the top of the plot represents the maximum field (angle or height). There are no units on the vertical scale because the plot is always normalized to the maximum radial field. The field curvature for the tangential and sagittal rays is defined as the distance from the defined image plane to the paraxial focus for that ray. If there is any defocus, then the two planes are not coincident, and so field curvature graphs too [24].

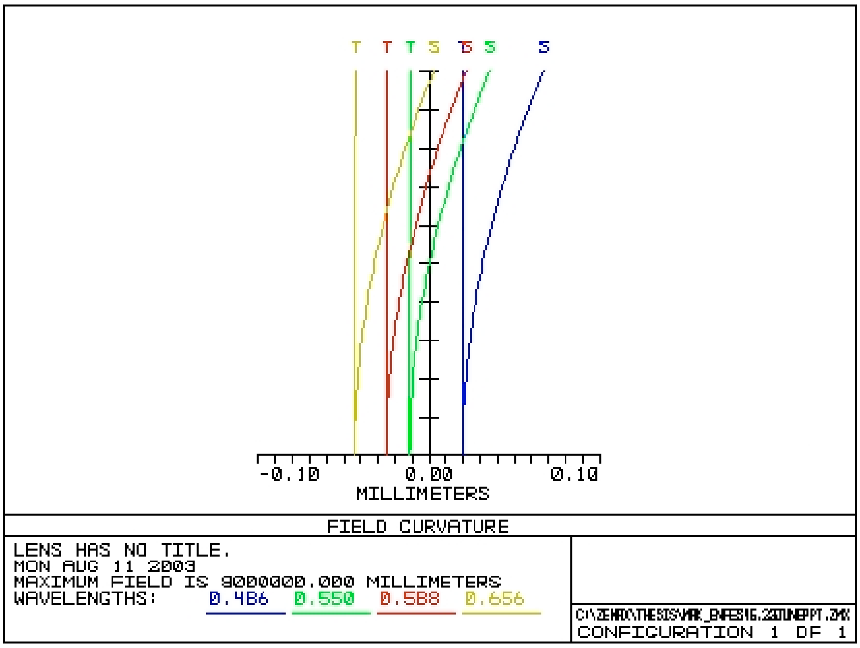

Figure 4.14. Field curvature of the designed camera for four wavelengths

Fig. (4.14.) shows the field curvature of the designed camera for four wavelengths. There is the defocus with 0.05 mm at the edge of the optical axis. Therefore, it is an insignificant effect for the designed system.

### 4.4. Distortion

There is a pincushion distortion as indicated Fig. (4.15) for the designed camera and its maximum value is only 0.0878% for the rays come from the center of the optical axis at wavelength 588 nm. Following figure also illustrates the maximum distortion, which has 0.2831% error, at the edge of the optical axis for this system. Although it is larger than the other value, it cannot affect the image quality so much.

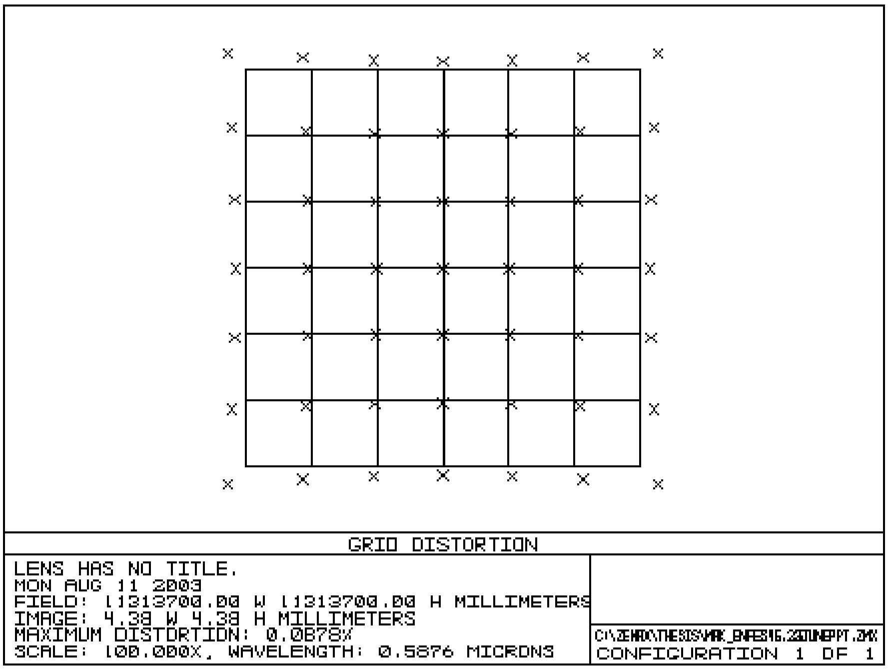

Figure 4.15. Distortion of the designed camera through of the optical axis

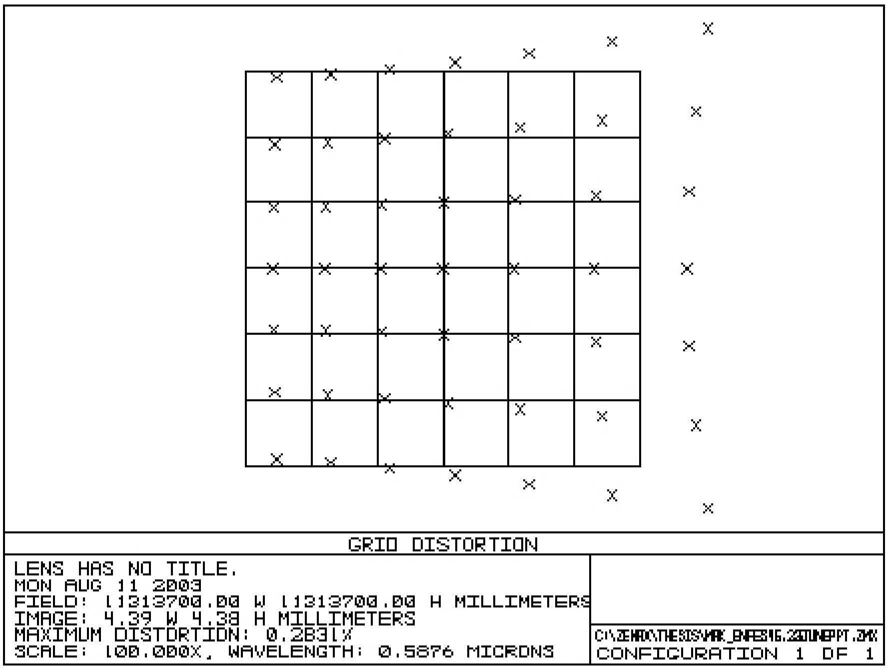

Figure 4.16. Distortion of the designed camera at the edge of the optical axis

## 4.5. Longitudinal Aberration

The spherical aberration of a system is usually represented graphically. Longitudinal spherical is plotted against the ray height at the lens or the optical system.

This feature computes the distance from the image surface to where a zonal marginal ray "focuses", or crosses the optical axis. The base of the plot is on axis, and the top of the plot represents the maximum entrance pupil radius. There are no units on the vertical scale because the plot is always normalized to the maximum entrance pupil radius. The horizontal scale is in lens units, and represents the distance from the image surface to the point where the ray crosses the optical axis.

Fig. (4.17) shows the longitudinal aberration of the designed camera for four wavelengths. Notice that the rays through only one zone of the system intersect the paraxial focus for the wavelengths 0.550 μm and 0.588 μm.

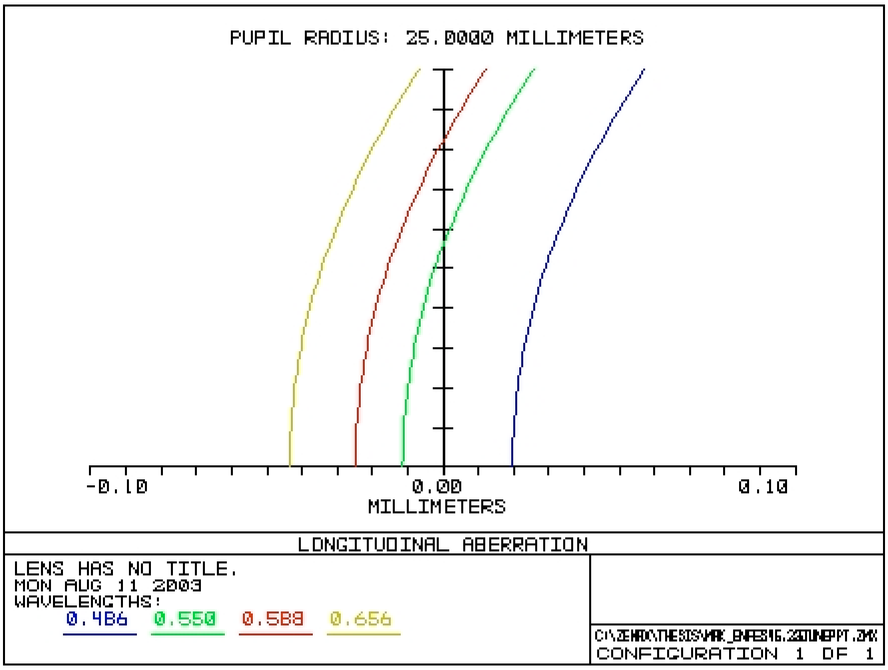

Figure 4.17. Longitudinal aberration for designed camera for four wavelengths

Following figure is simulated the longitudinal aberration for wavelength 0.588 μm for the designed system. It has been expanded many times.

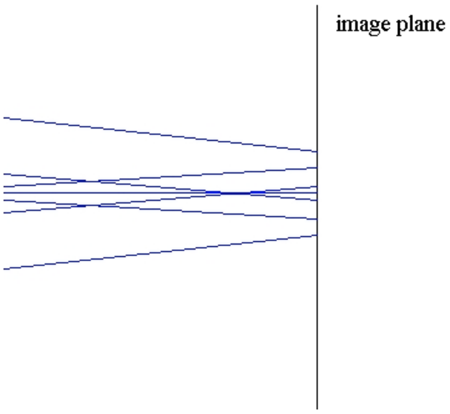

Figure 4.18. Focal plane simulation

## 4.6. Geometric Image Analysis

The total power in watts radiated by the source into the entrance pupil of the optical system. With the help of geometric image analysis, the total efficiency of this flux is computed.

The total efficiency of the power, which is detected by the designed camera, is approximately 85% see Fig. (4.19).

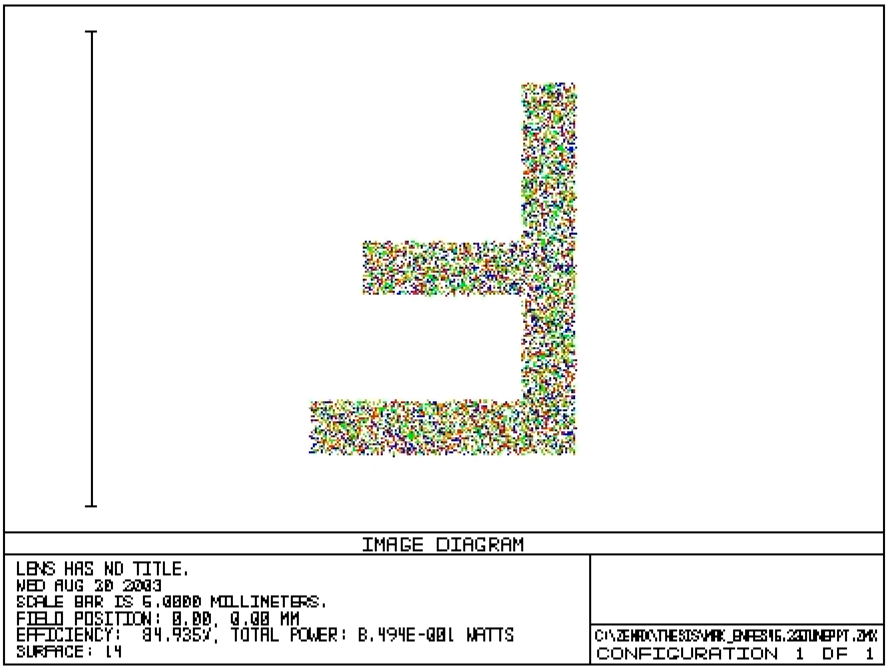

```
IMAGE DIAGRAM
LENS HAS NO TITLE.
WED AUG 20 2003
SCALE BAR IS 6.0000 MILLIMETERS.
FIELD POSITION: 0.00, 0.00 MM
EFFICIENCY:  84.935%, TOTAL POWER: 8.494E-001 WATTS
SURFACE: 14
[illegible]
CONFIGURATION 1 OF 1
```

Figure 4.19. Geometric image analysis of the designed camera

## 4.7. Diffraction Image Analysis

Diffraction image analysis defines the relative intensity at each of an arbitrary number of pixels arranged on a square grid. For example, the letter "F" may be described by a 7×7 grid such as:

0**11111**0
0**1**00000
0**1**00000
0**1111**00
0**1**00000
0**1**00000
0**1**00000

The image size parameter determines how big each pixel is in the image space of the optical system. This analysis defines the ideal image shape in image space. If the image size is 0.1 mm, then each pixel is 14.286 microns wide for this 7×7 pixels image.

The image size is 6.185 mm for the designed camera. It has been chosen 4096×4096 pixels CCD and each pixel of CCD is 3.631 microns wide as calculated in Sec. (3.3.1.1) for this system. According to the diffraction image analysis, the image size of the designed system takes the actual image size but each pixel is 883.629 microns wide for 7×7 pixels image that is the worst case for the image. Quality of image increases with the decreasing pixel size and the more number of pixels.

Fig. (4.20) illustrates the how the image is appeared for the rays coming from the center of the optical axis at 0.588 μm by the designed optical system. It shows the rate of aberrations with using a scale bar, which contains the number between 0 and 1. These numbers indicate the intensity at each pixel and pixels with a value of 0 do not radiate any rays.

The rays come from the edge of the optical axis in Fig. (4.21). As a result of this, effects of aberration and diffraction increase and the image blurs.

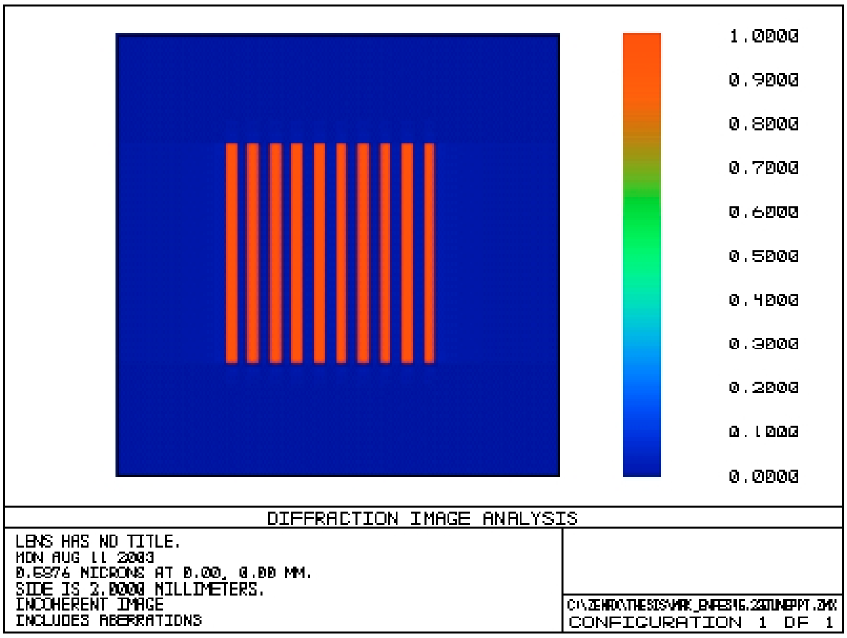

Figure 4.20. Diffraction image analysis of the designed camera through the optical axis

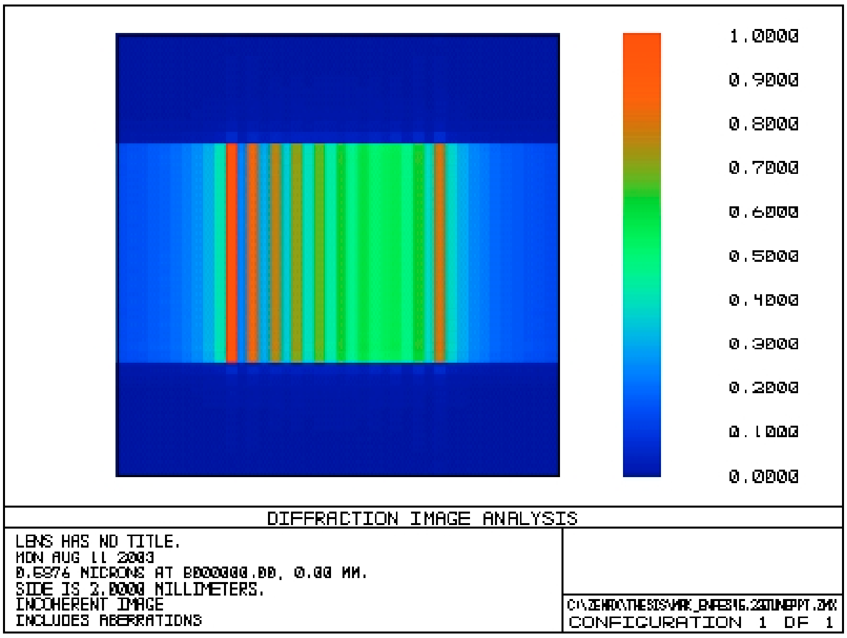

Figure 4.21. Diffraction image analysis of the designed camera at the edge of the optical axis

The diffraction-limited figure (see Fig.4.22) does not include the aberration. When this figure is compared to the Fig (4.20), there is not any difference, which one can observe. Therefore, if the designed camera gives better image for the worst cases as in discussed calculations of Sec. (3.3), it will provide the best images for the micro satellite remote sensing missions.

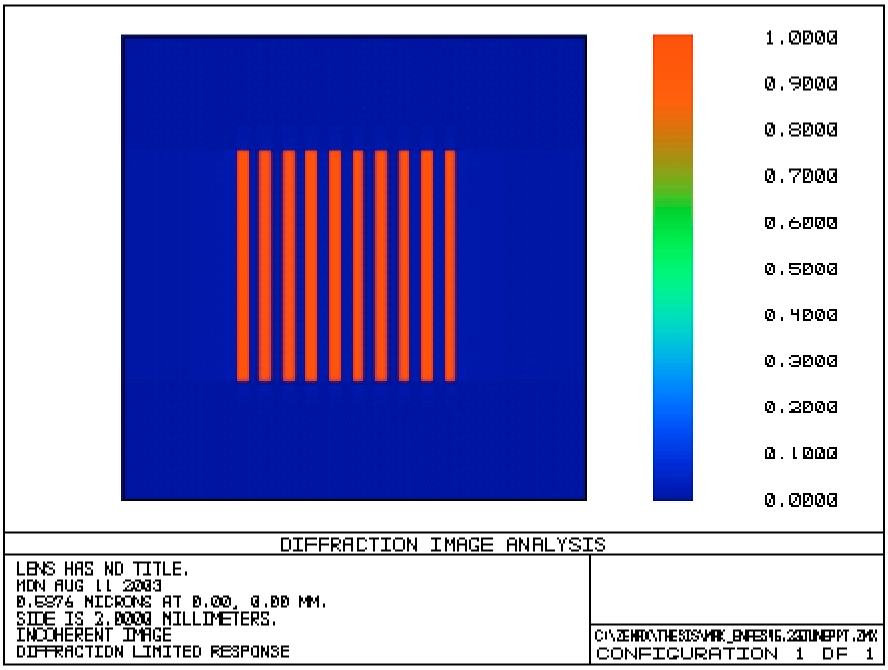

Figure 4.22. Diffraction image analysis for aberrationless condition

# CHAPTER 5

# DISCUSSION AND CONCLUSIONS

In this study, a camera system was designed to be used in a micro-satellite which is assumed on a circular orbit at an altitude of 600 km and take images of areas with 38.5×38.5 km from the earth surface. This designed camera system can be installed in a volume of 20×20×30 cm and its weight was found to be 71.911 g except the mechanical design. Therefore, the volume and the weight limitations sourced from micro-satellite were overcame.

The parameters like radius, thickness and type of glasses of the lenses and the mirrors, as well as the position of the lenses and the mirrors were simulated to obtain high quality images at the focal plane. These simulations were repeated several times for the different beam incident angles.

Also, parameters of the optical performance of this system (magnification, F-number, etc.), resolution, dimensions of CCD, integration time were calculated. Minimum longitudinal resolution, which is 9.394 m, of the designed system was limited by the Rayleigh criteria. The relation between the resolution and the wavelength was illustrated. Minimum pixel size of CCD, which can be used in this system, was found considering minimum resolution of the designed camera. When the CCD, which has the pixel size is less than the computed pixel size, uses for this designed optical system it cannot take the images effectively. The integration time and the velocity of the satellite with respect to Earth were computed in order to decrease the image-blur effects due to the motion of the satellite. The optimum values of CCD were defined from the computations for the designed camera. The incident total energy on each CCD pixel was computed for the visible region. From these computations, the numbers of electrons was calculated for each pixel during the integration time. This value is quite enough for imaging with high quality. Thus, the designed camera provides the sufficient energy to take the images. In addition, the environmental conditions such as, pressure and temperature at 600 km altitude were investigated and simulations of this design were performed at these conditions, but the influences of these effects on the optical materials were not considered.

Performance tests were obtained in order to understand the quality of the image, which is received from this designed camera. Modulation transfer function (MTF), point spread function (PSF), and spot diagrams were used in order to define the qualities of the image. Besides these, field curvature, longitudinal aberration and distortion values were simulated for the designed system. The total efficiency of the designed system was obtained by geometric image analysis. Diffraction effects for the designed optical system were observed by simulating diffraction image analysis. As a result of these analysis's and simulations, the image quality of this system was defined and it was concluded that this system can be used for micro-satellite's mission. Therefore, this camera, which shows good performance throughout various tests, can be installed in a micro-satellite.

# REFERENCES

[1] Fouquet, M., *Earth Imaging With Micro-Satellites: An Investigation, Implementation and In-Orbit Demonstration of Electronic Imaging Systems for Earth Observation On-Board Low-Cost Micro-satellites*, PhD, The University of Surrey, December 1995.

[2] Petrie, G. and Buyuksalih, G., *Aiming High Turkey's Efforts to Develop a Capability in Space Remote Sensing*, Geo Informatics, November 2001.

[3] Maksutov, D.D., *New Catadioptric Meniscus Systems*, Journal of the Optical Society of America (Vol. 34, Number 5), May 1944.

[4] Warren, J. Smith, *Modern Optical Engineering*, McGraw-Hill, 1990.

[5] www.ee.surrey.ac.uk/Research/CSER/UOSAT/papers/icdsc_ws/

[6] www.rosa.ro/romanian/documents/Volum/Session3/MN_SWEETING.htm

[7] Pedrotti, Frank L. and Pedrotti, Leno S., *Introduction To Optics*, Prentice-Hall PTR, 1996.

[8] Hecht, Eugene and Zajac, Alfred, *Optics*, Addison- Wesley Pub. Co., 1974.

[9] Melles Griot Catalog, *The Practical Application of Light*, 2000.

[10] Spindler & Hoyer Catalog, *Precision Optics*, 1989.

[11] Richards, O.W., *Consideration of Physical Optics, Optical Design*, Military Standardization Handbook, Defense Supply Agency Washington 25, D.C., 1962.

[12] Melles Griot Catalog, *Optics, Opto-Mechanics, Lasers, Instruments*, 1995/96.

[13] Larson, Wiley J. and Wertz, James R., *Space Mission Analysis and Design*, Second Edition, Microcosm, Inc. & Kluwer Academic Publishers, 1992.

[14] Kawada, Y., Takami, Y., Matsumura Y. and Fujita, T., *New Micro Satellite Concept For Observation Missions*, Acta Astronautica Vol. 46, Nos. 2-6, pp. 159-167, 2000.

[15] Royal Meteorological Institute of Belgium: Department of Aerology, http://remotesensing.oma.be/RadiometryPapers/article2.html, 2002.

[16] http://www.geol.vt.edu/profs/jas/pdf/4101-heat.prof, October 2002.

[17] http://www.earthmatrix.com/sciencetoday/solar-constant.html, July 2002.

[18] http://www.valdosta.edu/~grissino/

[19] Richards, John A., *Remote Sensing Digital Image Analysis An Introduction*, Springer-Verlag Berlin Heidelberg, 1986.

[20] Underwood, Craig and Unwin, Martin, *Spacecraft Design Project*, Lesson Notes University of Surrey Center for Satellite Engineering Research.

[21] Mende, S. B., Heetderks, H., Frey, H.U., Lampton, M., Geller, S. P., Abiad R., Siegmund, O.H.W., Tremsin, A.S., Spann, J., Dougani, H., Fuselier S. A., Magoncelli, A. L., Bumala, M.B., Murphree, S. and Trondsen, T., *Far Ultraviolet Imaging From The Image Spacecraft. 2. Wideband FUV Imaging*, Space Science Reviews 91: 271-285, 2000.

[22] Holst, Gerald C., *CCD Arrays, Cameras, and Displays*, SPIE Optical Engineering Press, 2nd Edition, 1998.

[23] Berry, Richard, *Choosing and Using a CCD Camera*, Willmann-Bell, Inc., 1992.

[24] ZEMAX Optical Design Program User's Guide Version 10.0, Focus Software, Inc., http://www.focus-software.com, 1990-2001.

[25] Walter, Ingo and Schönekeß, Jörg, *Application Of Micro-Mechanic Devices For Motion Compensation of Space-Borne CCD- Imaging Systems*, Acta Astronautica Vol. 46, Nos. 2-6, pp. 269-277, 2000.

[26] Ciccarelli, A., Davis, B., Jardin, W. Des, Doan, H., Meisenzahl, E., Pace, L., Putnam, G., Shepherd, J., Stevens, E., Summa, J. and Wetzel, K., *Front-illuminated full-frame charge-coupled device image sensor achieves 85% peak quantum efficiency*, Eastman Kodak Company, Rochester, NY 14650-2010, 1999.

[27] Schroeder, Daniel J., *Astronomical Optics*, Academic Press, 2nd Edition, 2000.

[28] Richards, E. Hopkins, Hanau, Richard, *Aberration Analysis And Third Order Theory,* Military Standardization Handbook, Defense Supply Agency Washington 25, D.C., 1962.

[29] Fischer, R. E., *Optical Design: Principles of Optical Systems Layout*, SPIE-The International Society for Optical Engineering, 1993.

[30] Goody, Richard M. and Yung, Y.L., *Atmospheric Radiation Theoretical Basis*, Oxford University Press, 2nd Edition, 1989.

# APPENDIX A

# PERFORMANCE FACTORS OF OPTICAL SYSTEMS

The performance of real optical systems is limited by several factors, including lens aberrations and light diffraction. Numerous other factors, such as lens manufacturing tolerances and component alignment, impact the performance of an optical system. However, these are not considered explicitly in the following discussion [9].

## A.1. Diffraction

Diffraction, a natural property of light arising from its wave nature, poses a fundamental limitation on any optical system. Diffraction is always present, although its effects may be masked if the system has significant aberrations. When an optical system is essentially free from aberrations, its performance is limited solely by diffraction, and it is referred to as diffraction limited.

In all light beams, some energy is outside the region predicted by rectilinear propagation. This effect, known as diffraction, is a fundamental and inescapable physical phenomenon.

Diffraction effects are traditionally classified into either Fresnel or Fraunhofer types. Fresnel diffraction is primarily concerned with what happens to light in the immediate neighborhood of a diffracting object or aperture. It is thus only of concern when the illumination source is close to this aperture or object. Consequently, Fresnel diffraction is rarely important in most optical setups.

Fraunhofer diffraction, however, is often very important. This is the light-spreading effect of an aperture when the aperture (or object) is illuminated with an infinite source (plane-wave illumination) and the light is sensed at an infinite distance (far-field) from this aperture.

From these simple definitions, one might assume that Fraunhofer diffraction is important only in optical systems with infinite conjugate, whereas Fresnel diffraction equations should be considered at finite conjugate ratios. Not so!. A lens or lens system of finite positive focal length with plane-wave input maps the far-field diffraction pattern of its aperture onto the focal plane; therefore, it is Fraunhofer diffraction that determines the limiting performance of optical systems. More generally, at any conjugate ratio, far-field angles are transformed into spatial displacements in the image plane [9].

The goal in designing a lens system on the basis of geometrical optics is to find a combination of lenses for which all rays in a specified cone of rays that diverges from an object point P are converged upon the corresponding image point $P'$ such that the optic paths of all rays from P to $P'$ are equal. Other requirements are added. For example, it may be required that points P to $P'$ shall belong to a single object plane and a single image plane, respectively. Even when the design satisfies all these requirements to a high degree, the image $P'$ of a self-luminous object point P is not a point but consists of a central bright spot surrounded by systematically distributed dark and bright fringes whose contour and width depend upon the contour and dimensions of the aperture of the lens. If, for example, the lens aperture is circular and if the self-luminous object point is located upon or near the optic axis, the image consists of a circular, central bright spot surrounded alternately by dark and bright rings. The central bright spot is called the airy disc, in Fig. (A.1). Its diameter decreases as the diameter of the lens aperture is increased. The far-field angular radius of the airy disc, is very nearly

$$\Delta\theta = \frac{1.22\lambda}{D} \qquad \text{(A.1)}$$

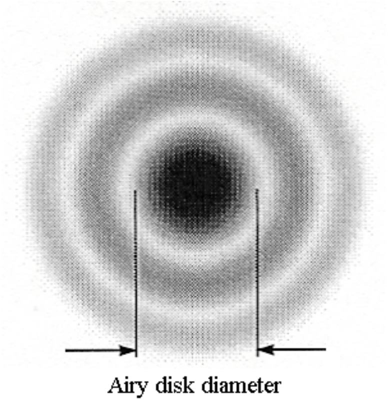

Figure A.1. Airy disc diameter [9]

The actual image of the object point is modified to such a degree by diffraction from the finite lens aperture that this image is appropriately called a diffraction image.

The diffractive nature of the image may not be so apparent with, for example, high-speed objectives in which compromises among the geometrical corrections and tolerable aberrations must be made. However, the image will generally exhibit effects due to diffraction, i.e., effects that cannot be explained from Snell's law of refraction and reflection alone. In any case, the image of a point will not be a point; an exact point-by-point similarity between object and image cannot be achieved. Resolution of details in the image of the object is restricted first by degree of correction of the optical system and finally by the laws of diffraction, i.e., by the laws governing the bending of light rays from the paths consistent with Snell's law of refraction and reflection.

Broadly, diffraction is the phenomenon whereby waves are modified in direction, amplitude, and in phase by interaction with an object or obstacle. In its most general sense, diffraction includes the phenomena of refraction and reflection but these two phenomena are ordinarily considered apart from diffraction. However, when the dimensions of the object become comparable to the wavelength, the concepts of refraction and reflection become useless. With such small objects, even scattering becomes a direct aspect of diffraction [11].

## A.2. Aberrations

To determine the precise performance of a lens, one can trace the path of light rays through it, using Snell's law at each optical interface to determine the subsequent ray direction. This process, called ray tracing, is usually accomplished on a computer. When this process is completed, it is typically found that not all the rays pass through the points or positions predicted paraxial theory. These deviations from ideal imaging are called lens aberrations.

The direction of a light ray, after refraction at the interface between two homogeneous, isotropic media of differing index of refraction, is given by Snell's law,

$$n_1 \sin\theta_1 = n_2 \sin\theta_2 \tag{A.2}$$

where $\theta_1$ is the angle of incidence, $\theta_2$ is the angle of refraction, and both angles are measured from the surface normal as shown in Fig. (A.2).

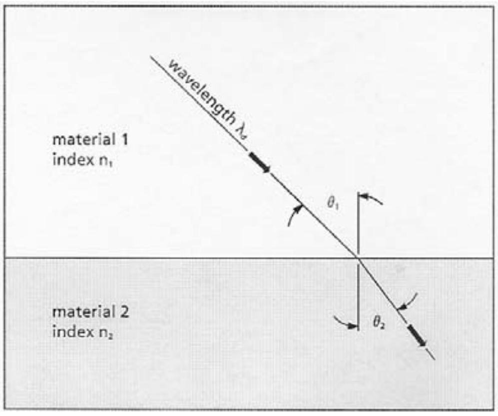

Figure A.2. Refraction of light at a dielectric boundary [9]

Even though tools for precise analysis of an optical system are becoming easier to use and are readily available, it is still quite useful to have a method for quickly estimating lens performance. This not only saves time in the initial stages of system specification, but can also help achieve a better starting point for any further computer optimization.

The first step in developing these rough guidelines is to realize that the sine functions in Snell's law can be expanded in an infinite Taylor series:

$$\sin\theta = \theta_1 - \theta_1^3/3! + \theta_1^5/5! - \theta_1^7/7! + \theta_1^9/9! - \dots \qquad (A.3)$$

The first approximation one can make is to replace all sine functions with their arguments (i.e., replace $\sin\theta_1$ with $\theta_1$ itself and so on). This is called first-order or paraxial theory because only the first terms of the sine expansions are used. Design of any optical system generally starts with this approximation using the paraxial formulas.

The assumption that $\sin\theta = \theta$ is reasonably valid for $\theta$ close to zero (i.e., high f-number lenses). With more highly curved surfaces (and particularly marginal rays), paraxial theory yields increasingly large deviations from real performance because

$\sin\theta \neq \theta$. These deviations are known as aberrations. Because a perfect optical system (one without any aberrations) would form its image at the point and to the size indicated by paraxial theory, aberrations are really a measure of how the image differs from the paraxial prediction.

As already stated, exact ray tracing is the only rigorous way to analyze real lens surfaces. Before the advent of computers, this was excessively tedious and time consuming. Seidel addressed this issue by developing a method of calculating aberrations resulting from the $\theta_1^3/3!$ term. The resultant third-order lens aberrations are therefore called Seidel aberrations.

To simplify these calculations, Seidel put the aberrations of an optical system into several different classifications. In monochromatic light they are spherical aberration, astigmatism, field curvature, coma, and distortion. In polychromatic light there are also chromatic aberration and lateral color. Seidel developed methods to approximate each of these aberrations without actually tracing large numbers of rays using all the terms in the sine expansions [9].

### A.3. Spherical Aberration

Figure (A.3) illustrates how an aberration-free lens focuses incoming collimated light. All rays pass through the focal point F". The lower figure shows the situation more typically encountered in single lenses. The farther from the optical axis the ray enters the lens, the nearer to the lens it focuses (crosses the optical axis). The distance along the optical axis between the intercept of the rays that are nearly on the optical axis (paraxial rays) and the rays that go through the edge of the lens (marginal rays) is called longitudinal spherical aberration (LSA). The height at which these rays intercept the paraxial focal plane is called transverse spherical aberration (TSA). These quantities are related by

$$\mathrm{TSA} = \mathrm{LSA} \times \tan u'' \qquad \text{(A.4)}$$

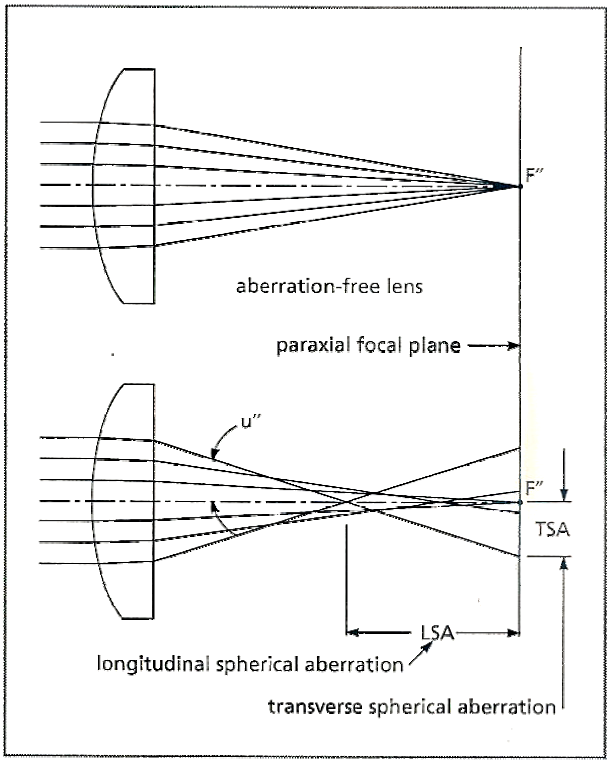

Figure A.3. Spherical aberration of a plano-convex lens [9]

Spherical aberration is dependent on lens shape, orientation, and conjugate ratio, as well as on the index of refraction of the materials present. Fortunately, these aberrations can be virtually eliminated by combining the effects of two or more spherical surfaces. In general, simple positive lenses have undercorrected spherical aberration, and negative lenses usually have overcorrected spherical aberration. By combining a positive lens made from low-index glass with a negative lens made from high-index glass, it is possible to produce a combination in which the spherical aberrations cancel but the focusing powers do not [9].

## A.5. Coma

In spherical lenses, different parts of the lens surface exhibit different degrees of magnification. This gives rise to an aberration known as coma. As shown in Fig. (A.4), each concentric zone of a lens forms a ring-shaped image called a comatic circle. This causes blurring in the image plane of off-axis object points. An off-axis object point is not a sharp image point, but it appears as a characteristic comet-like flare.

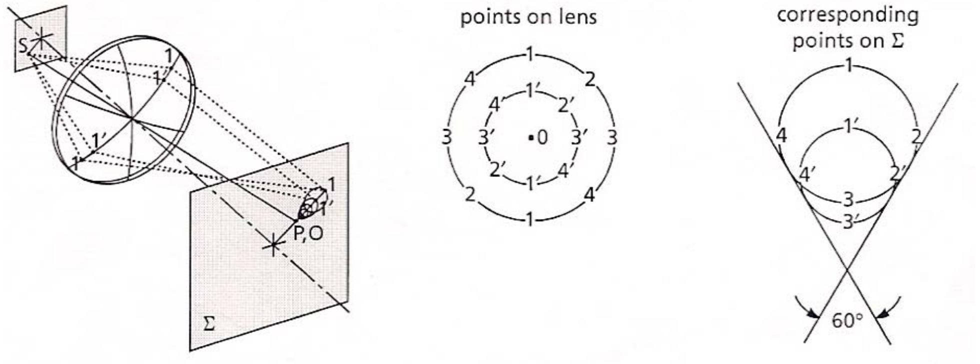

Figure A.4. Imaging an off-axis point source by a lens with positive transverse coma [9]

Even if spherical aberration is corrected and the lens brings all rays to a sharp focus on axis, a lens may still exhibit coma off axis. See Fig. (A.5).

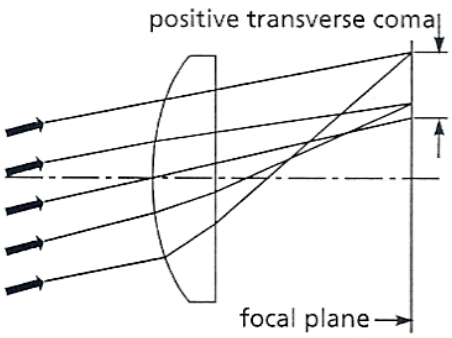

Figure A.5 Positive transverse coma [9]

As with spherical aberration, correction can be achieved by using multiple surfaces. Alternatively, a sharper image may be produced by judiciously placing an aperture, or stop, in an optical system to eliminate the more marginal rays [9].

### A.4. Astigmatism and Field Curvature

When an off-axis object is focused by a spherical lens, the natural asymmetry leads to astigmatism. The system appears to have two different focal lengths.

As shown in Fig. (A.6), the plane containing both optical axis and object point is called the tangential plane. Rays that lie in this plane are called meridional or tangential rays. Rays not in this plane are referred to as skew rays. The chief, or principal, ray goes from the object point through the center of the aperture of the lens system. The plane perpendicular to the tangential plane that contains the principal ray is called the sagittal or radial plane.

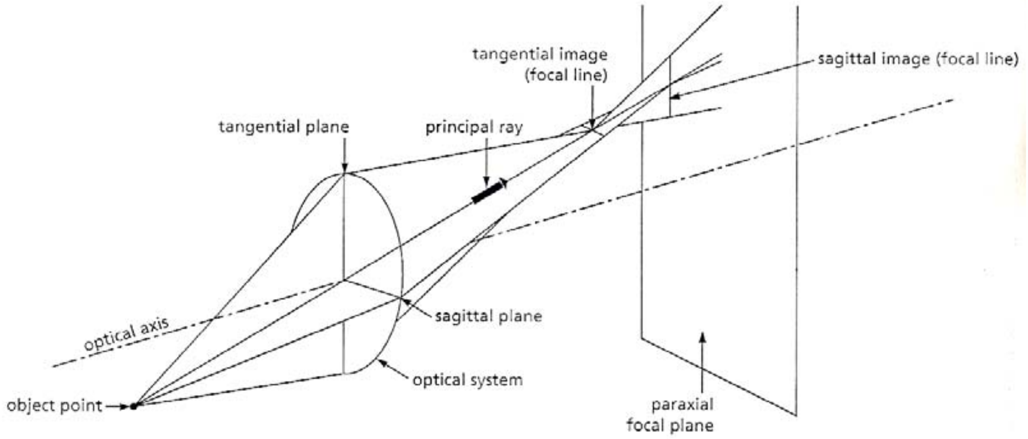

Figure A.6. Astigmatism represented by sectional views [9]

The figure illustrates that tangential rays from the object come to a focus closer to the lens than do rays in the sagittal plane. When the image is evaluated at the tangential conjugate, a line in the sagittal direction is seen. A line in the tangential direction is formed at the sagittal conjugate. Between these conjugates, the image is either an elliptical or a circular blur. Astigmatism is defined as the separation of these conjugates [9].

Unless a lens is poorly made, there is no astigmatism when an axial point is imaged. As the imaged point moves further from the axis, the amount of astigmatism gradually increases. Off-axis images seldom lie exactly in a true plane; when there is primary astigmatism in a lens system, the images lie on curved surfaces, which are paraboloid in shape. The shape of these image surfaces is indicated for a simple lens in Fig. (A.7) [4].

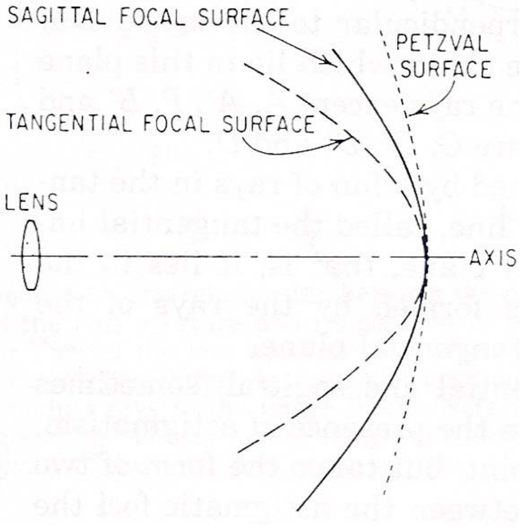

Figure A.7. The primary astigmatism of a simple lens [4]

The amount of astigmatism in a lens depends on lens shape only when there is an aperture in the system that is not contact with the lens itself. Astigmatism strongly depends on the conjugate ratio [9].

Every optical system has associated with it a sort of basic field curvature, called Petzval curvature, which is a function of the index of refraction of the lens elements and their surface curvatures. When there is no astigmatism, the sagittal and tangential image surfaces coincide with each other and lie on the Petzval surface. When there is primary astigmatism present, the tangential image surface lies three times as far from the Petzval surface as the sagittal image; note that both image surfaces are on the same side of the Petzval surface, as indicated in Fig. (A.7).

When the tangential image is to the left of the sagittal image (and both are to the left of the Petzval surface) the astigmatism is called negative, undercorrected, or inward- (toward the lens) curving. When the order is reversed, the astigmatism is overcorrected, or backward-curving In Fig. (A.7), the astigmatism is under-corrected and all three surfaces are inward-curving.

Positive lenses introduce inward curvature of the Petzval surface to a system, and negative lenses introduce backward curvature. Petzval curvature (i.e., the longitudinal departure of the Petzval surface from the ideal flat image surface) of a thin simple element is equal to the square of image height divided by the focal length and index of the element [4].

### 4.6 Distortion

The image field not only may have curvature but may also be distorted. The image of an off-axis point may be formed at a location on this surface other than that predicted by the simple paraxial equations. This distortion is different from coma. Distortion means that even if a perfect off-axis point fail to meet perfectly in the image is formed, its location on the image plane is not correct. Furthermore, the amount of distortion usually increases with increasing image height. The effect of this can be seen as two different kinds of distortion: pincushion and barrel (see Fig.A.8). Distortion does not lower system resolution; it simply means that the image shape does not correspond exactly to the shape of the object. Distortion is a separation of the actual image plane and can be expressed either as an absolute value or as a percentage of the paraxial image height.

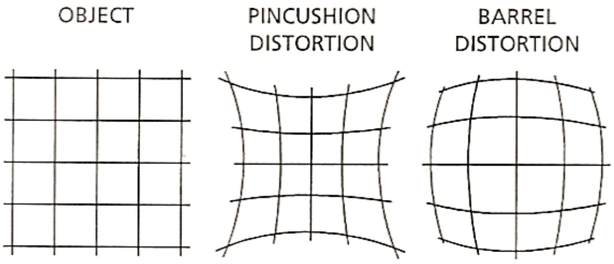

Figure A.8 Pincushion and barrel distortion [9]

It should be apparent that a lens or lens system has opposite types of distortion depending on whether it is used forward or backward. This means that if a lens were used to make a photograph, and then used in reverse to project it, there would be no distortion in the final screen image [9].

### 4.7 Chromatic Aberration

The aberrations previously described are purely a function of the shape of the lens surfaces, and can be observed with monochromatic light. There are, however, other aberrations that arise when these optics are used to transform light containing multiple wavelengths.

The index of refraction of a material is a function of wavelength, known as dispersion. From Snell's law, it can be seen that light rays of different wavelengths or colors will be refracted at different angles since the index is not constant. Figure A.9. shows the result when polychromatic collimated light is incident on a positive lens element. Because the index of refraction is higher for shorter wavelengths, these are focused closer to the lens than the longer wavelengths. Longitudinal chromatic aberration is defined as the axial distance from the nearest to the farthest focal point.

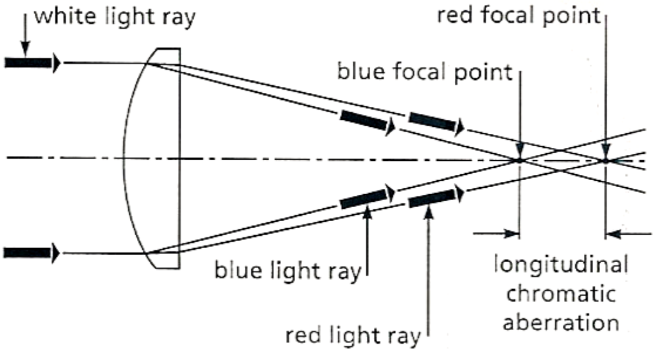

Figure A.9. Longitudinal chromatic aberration [9]

As in the case of spherical aberration, positive and negative elements have opposite signs of chromatic aberration. Once again, by combining elements of nearly opposite aberration to form a doublet, chromatic aberration can be partially corrected. It is necessary to use two glasses with different dispersion characteristics, so that the weaker negative element can balance the aberration of the stronger, positive element [9][*].

---

[*] A simple converging lens, which is necessarily uncorrected for aberrations, is said to be undercorrected. When a particular aberration is made zero, or smaller than some predetermined tolerance, the lens system is said to be corrected. If the aberration of the system has a sign opposite to that of a simple converging lens, the system is overcorrected [28].

# APPENDIX B

# CALCULATION OF THE IMAGE POINT

This appendix deals with methods of analyzing optical systems when they become complex, involving a number of refracting and/or reflecting elements in trainlike fashion. Beginning with a description of a single thick lens in terms of its cardinal points, the discussion proceeds to an analysis of a train of optical elements by means of 2×2 matrices representing the elementary refractions or reflections involved in the train. In this way, a system matrix for the entire optical system can be found that is related to the same cardinal points characterizing the thick lens. Finally, computer ray-tracing methods for tracing a given ray of light through an optical system are briefly described.

## B.1. The Thick Lens

Consider a spherical thick lens, that is, a lens whose thickness along its optical axis cannot be ignored without leading to serious errors in analysis. The glass medium is bounded by two spherical refracting surfaces. The image of a given object, formed by refraction at the first surface, becomes the object for refraction at the second surface. The object distance for the second surface takes into account the thickness of the lens. The image formed by the second surface is then the final image due to the action of the composite thick lens.

The thick lens can also be described in a way that allows graphical determination of images corresponding to arbitrary objects. This description, in terms of the so-called cardinal points of the lens, is useful also because it can be applied to more complex optical systems.

There are six cardinal points on the axis of a thick lens, from which its imaging properties can be deduced. Planes normal to the axis at these points are called the cardinal planes. The six cardinal points consist of the first and second system focal points ($F_1$ and $F_2$), which are already familiar; the first and second principal points ($H_1$ and $H_2$); and the first and second nodal points ($N_1$ and $N_2$).

The positions of all six cardinal points are indicated in Fig. (B.1). Distances are directed, positive or negative by a sign convention that makes distances directed to the left negative and distances to the right, positive. Notice that for the thick lens, the distances $r$ and $s$ determine the positions of the principal points relative to the vertices $V_1$ and $V_2$, while $f_1$ and $f_2$ determine focal point positions relative to the principal points.

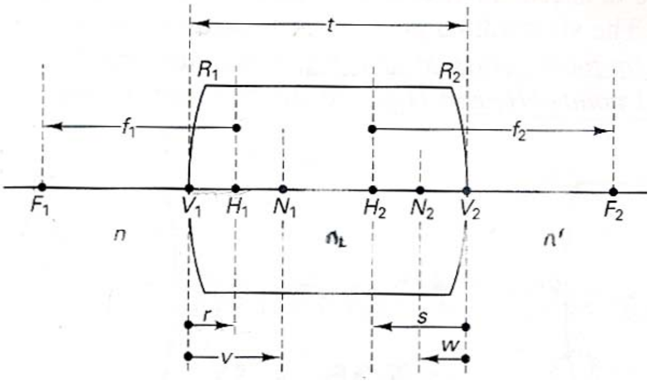

Figure B.1. Positions of the all six cardinal points

Utilizing the symbols defined in Fig. (B.1), the focal length $f_1$ is given by

$$\frac{1}{f_1} = \frac{n_L - n'}{nR_2} - \frac{n_L - n}{nR_1} - \frac{(n_L - n)(n_L - n')}{nn_L}\frac{t}{R_1 R_2} \tag{B.1}$$

and the focal length $f_2$ is conveniently expressed in terms of $f_1$ by

$$f_2 = -\frac{n'}{n} f_1 \qquad \text{(B.2)}$$

The principal planes can be located

$$r = \frac{n_L - n'}{n_L R_2} f_1 t \quad \text{and} \quad s = -\frac{n_L - n}{n_L R_1} f_2 t \qquad \text{(B.3)}$$

The positions of the nodal points are given by

$$v = \left(1 - \frac{n'}{n} + \frac{n_L - n'}{n_L R_2} t\right) f_1 \qquad \text{and} \qquad w = \left(1 - \frac{n}{n'} - \frac{n_L - n}{n_L R_1} t\right) f_2 \qquad \text{(B.4)}$$

Image and object distances and lateral magnification are related by

$$-\frac{f_1}{s_o} + \frac{f_2}{s_i} = 1 \qquad \text{and} \qquad m = -\frac{n s_i}{n' s_o} \qquad \text{(B 5)}$$

as long as the distances $s_o$ (object point) and $s_i$ (image point), as well as focal lengths, are measured relative to corresponding principal planes.

### B.2. The Matrix Method

When the optical system consists of several elements –for example, the four or five lenses that constitute a photographic lens– a systematic approach that facilitates analysis is needed. This systematic approach is well handled by the matrix method. By combining matrices that represent individual refractions and reflections, a given optical system may be represented by a single matrix, from which the essential properties of the composite optical system may be deduced. The method lends itself to computer techniques for tracing a ray through an optical system of arbitrary complexity.

## B.3. Some Simple Ray-Transfer Matrices

1. Translation Matrix:

$$M = \begin{bmatrix} 1 & d \\ 0 & 1 \end{bmatrix}$$

2. Refraction at a Planar Boundary:

$$M = \begin{bmatrix} 1 & 0 \\ 0 & n_1/n_2 \end{bmatrix}$$

3. Refraction at a Spherical Boundary: Convex $R > 0$; Concave $R < 0$:

$$M = \begin{bmatrix} 1 & 0 \\ -\dfrac{(n_2 - n_1)}{n_2 R} & \dfrac{n_1}{n_2} \end{bmatrix}$$

4. Refraction Through a Thin Lens: Convex $f > 0$; Concave $f < 0$:

$$M = \begin{bmatrix} 1 & 0 \\ -1/f & 1 \end{bmatrix}$$

5. Reflection From a Planar Mirror:

$$M = \begin{bmatrix} 1 & 0 \\ 0 & 1 \end{bmatrix}$$

6.Reflection From a Spherical Mirror:

$$M = \begin{bmatrix} 1 & 0 \\ 2/R & 1 \end{bmatrix}$$

## B.4. System Ray-Transfer Matrix

By combining appropriate individual matrices in the proper order, it is possible to express any optical system by a single 2×2 matrix, which is called the system matrix.

Generalizing, the matrix equation representing any number N of translations, reflections, and refractions is given by

$$\begin{bmatrix} y_f \\ \alpha_f \end{bmatrix} = M_N M_{N-1} \ldots M_2 M_1 \begin{bmatrix} y_0 \\ \alpha_0 \end{bmatrix} \qquad \text{(B.6)}$$

and the ray-transfer matrix representing the entire optical system is

$$M = M_N M_{N-1} \ldots M_2 M_1 \qquad \text{(B 7)}$$

When this method is applied on designed micro satellite camera, it is found as

$$M := R_7 \cdot T_8 \cdot R_6 \cdot T_7 \cdot R_5 \cdot T_6 \cdot \mathrm{Refl}_2 \cdot T_5 \cdot \mathrm{Refl}_1 \cdot T_4 \cdot R_4 \cdot T_3 \cdot R_3 \cdot T_2 \cdot R_2 \cdot T_1 \cdot R_1$$

$$R_1 := \begin{bmatrix} 1 & 0 \\ \dfrac{-0.5168}{(-2310)\cdot 1.5168} & \dfrac{1}{1.5168} \end{bmatrix}$$

$$T_1 := \begin{pmatrix} 1 & 5 \\ 0 & 1 \end{pmatrix}$$

$$R_2 := \begin{bmatrix} 1 & 0 \\ \dfrac{0.5168}{(-558)\cdot 1} & 1.5168 \end{bmatrix}$$

$$T_2 := \begin{pmatrix} 1 & 7.05 \\ 0 & 1 \end{pmatrix}$$

$$R_3 := \begin{bmatrix} 1 & 0 \\ \dfrac{-0.5168}{(-659)\cdot 1.5168} & \dfrac{1}{1.5168} \end{bmatrix}$$

$$T_3 := \begin{pmatrix} 1 & 5 \\ 0 & 1 \end{pmatrix}$$

$$R_4 := \begin{bmatrix} 1 & 0 \\ \dfrac{0.5168}{(-10000)\cdot 1} & \dfrac{1.5168}{1} \end{bmatrix}$$

$$T_4 := \begin{pmatrix} 1 & 100 \\ 0 & 1 \end{pmatrix}$$

$$\mathrm{Refl}_1 := \begin{bmatrix} 1 & 0 \\ \dfrac{2}{(-405)} & 1 \end{bmatrix}$$

$$T_5 := \begin{pmatrix} 1 & -100 \\ 0 & 1 \end{pmatrix}$$

$$\mathrm{Refl}_2 := \begin{bmatrix} 1 & 0 \\ \dfrac{2}{(-10000)} & 1 \end{bmatrix}$$

$$T_6 := \begin{pmatrix} 1 & 100 \\ 0 & 1 \end{pmatrix}$$

$$R_5 := \begin{bmatrix} 1 & 0 \\ \dfrac{-0.6889}{(-40)\cdot 1.6889} & \dfrac{1}{1.6889} \end{bmatrix}$$

$$T_7 := \begin{pmatrix} 1 & 1.5 \\ 0 & 1 \end{pmatrix}$$

$$R_6 := \begin{bmatrix} 1 & 0 \\ \dfrac{(1.6889 - 1.5168)}{(85)\cdot 1.6889} & \dfrac{1.6889}{1.5168} \end{bmatrix}$$

$$T_8 := \begin{pmatrix} 1 & 1.5 \\ 0 & 1 \end{pmatrix}$$

$$R_7 := \begin{bmatrix} 1 & 0 \\ \dfrac{0.5168}{(-300)\cdot 1} & 1.5168 \end{bmatrix}$$

$$M = \begin{pmatrix} 0.9922 & 117.3230 \\ 0.0115 & 2.3742 \end{pmatrix}$$

Image point of the designed camera is calculated as follow,

$$\begin{pmatrix} 1 & s \\ 0 & 1 \end{pmatrix} \cdot \begin{pmatrix} 0.9922 & 117.3230 \\ 0.0115 & 2.3742 \end{pmatrix}$$

S = 49.4147 mm

# APPENDIX C

# F-NUMBERS OF THE DESIGNED CAMERA

There are three types of F-number that are calculated by Zemax:

Image space F/# is the ratio of the paraxial effective focal length calculated at infinite conjugates over the paraxial entrance pupil diameter.

The paraxial working F/# is defined as, where is the paraxial marginal ray angle in image space and n is the index of refraction of image space. The paraxial marginal ray is traced at the specified conjugates. The paraxial working F/# is the effective F/# ignoring aberrations.

Working F/# is defined as, where is the marginal ray angle in image space and n is the index of refraction of image space. The marginal ray is traced at the specified conjugates. Working F/# is generally much more useful than image space F/# because it is based upon real ray data at the actual conjugates of the lens.
Although there are numerous simple formulas for computing paraxial entities, such as focal length, F/#, magnification, etc., ZEMAX generally does not use these formulas. Internally, ZEMAX traces "parabasal" rays, which are real (real means using Snell's law explicitly) that make small angles with respect to the base ray, which is usually an axis or chief ray. Parabasal rays rather than paraxial formulas is used by Zemax, because so many optical systems include non-paraxial components, which are not well described by conventional axial first-order theory. This includes tilted or decentered systems, and systems using holograms,

diffractive optics, general aspheres, and gradient index lenses [24]. As a result of this, result of the calculations based on theory of optics which is applied in this thesis will not same as Zemax results exactly.

The F-number of this system is given by

$$\frac{f}{D} = \frac{231.9524\times10^{-3}}{60\times10^{-3}} = 3.865 \tag{C.1}$$

This result is exactly same as the Image space F/# in Zemax and it is used in the optics books.

As an example, it is considered primary parabolic mirror in this design, its Image space F/# and Working F/# have been found as follows:

R = 405 mm
f = 202.5 mm
D = 60 mm
Image space F/# = $\frac{f}{D} = \frac{202.5}{60} = 3.375$

Working F/# probably depends on the shape of the mirror. A parabolic mirror's surface is defined by the equation $y^2 = 4fx$ as discussed beginning of this chapter.
$y$ = 30 mm because of the Cartesian coordinate system

$30^2 = 4\times(202.5)\,x$
$x = 1.\overline{11}\,\text{mm}$
$f + x = 203.6\overline{11}\,\text{mm}$

$$\text{Working F/\#} = \frac{f+x}{D} = 3.393 \tag{C.2}$$

This results corresponds the Zemax, exactly for primary parabolic mirror. When same method has been applied for the camera system, working F/# has been found as 3.882. However, Zemax has calculated 3.896. The reason difference between two calculations is because it has been supposed there is only one parabolic mirror but there are two parabolic mirrors and spherical lenses in this system. These parts of system affect the working F/#.

# APPENDIX D

# PRESCRIPTION DATA FOR DESIGNED CAMERA

## D.1. Data For Section (3.3.1)

Effective Focal Length: -231.9524 mm (in air)

Effective Focal Length: -231.9524 mm (in image space)

Back Focal Length: -4.56526 mm

Total Track: 154.6402 mm

Image Space F/#: 4.639047

Paraxial Working F/#: 4.639056

Working F/#: 4.66481

Image Space NA: 0.1071599

Object Space NA: 4.166666e-008

Stop Radius: 24.96669 mm

Paraxial Image Height: 3.092703 mm

Paraxial Magnification: -3.865879e-007

Entrance Pupil Diameter: 50 mm

Entrance Pupil Position: -144.224 mm

Exit Pupil Diameter: 10.96708 mm

Exit Pupil Position: -50.9017 mm

Maximum Field: 8000000 mm

Primary Wave: 0.5875618 µm

Angular Magnification: -4.559098

## D.2. Data Contains Values Of Pressure And Temperature

Altitude (km): 600
Temperature (K): 999.850
Pressure (mb): $8.2130 \times 10^{-10}$
Density (g cm$^{-3}$): $1.1370 \times 10^{-16}$
Pressure Scale Height (km): 88.2440
Number Density (cm$^{-3}$): $5.9500 \times 10^{6}$
Molecular Weight (amu): 11.510 [30]

Temperature (C): 7.26850E+002
Pressure (ATM): 8.1050E-013
Effective Focal Length: -231.9609 mm (in air)
Effective Focal Length: -231.9544 mm (in image space)
Back Focal Length: -4.5728 mm
Total Track: 154.6402 mm
Image Space F/#: 4.639218
Paraxial Working F/#: 4.639226
Working F/#: 4.664976
Image Space NA: 0.107156
Object Space NA: 4.166666e-008
Stop Radius: 24.96644 mm
Paraxial Image Height: 3.092817 mm
Paraxial Magnification: -3.866021e-007
Entrance Pupil Diameter: 50 mm
Entrance Pupil Position: -144.2163 mm
Exit Pupil Diameter: 10.97688 mm
Exit Pupil Position: -50.94149 mm
Maximum Field: 8000000 mm
Primary Wave: 0.5875618 µm
Angular Magnification: -4.555028